

Cite this: *J. Mater. Chem. A*, 2024, 12, 30971

# Advances in sodium-ion battery cathode materials: exploring chemistry, reaction mechanisms, and prospects for next-generation energy storage systems

Han Zhang,<sup>a</sup> Liguang Wang <sup>\*b</sup> and Pengjian Zuo <sup>\*c</sup>

Lithium-ion batteries (LIBs) have been powering portable electronic devices and electric vehicles for over three decades. However, growing concerns regarding the limited availability of lithium resources and the subsequent surge in costs have prompted the exploration of alternative energy storage systems beyond LIBs. Among these alternatives, sodium-based batteries, with their similar intercalation chemistry, have emerged as the most promising alternative due to their cost-effectiveness and the abundance of sodium reserves in nature. Developing sodium-ion batteries (SIBs) that possess high energy density, long lifespan, and high-rate capability necessitates a comprehensive understanding of the reaction mechanisms, especially the intricate chemistry involved in cathode materials. In this review, we delve into the reaction mechanisms of the most commonly used cathode materials for SIBs, which include layered transition-metal oxides, polyanionic compounds, Prussian blue analogues, etc. We also highlight the specific physicochemical properties that have been uncovered through the application of advanced *operando* characterization techniques. Building upon the insights gained from this comprehensive review, we put forth future perspectives on the development of novel cathode materials for SIBs. By leveraging the extensive knowledge generated, we aspire to pave the way for further advancements in sodium-ion battery technology.

Received 30th May 2024  
Accepted 18th October 2024

DOI: 10.1039/d4ta03748k

rsc.li/materials-a

## 1. Introduction

Over the past decade, the escalating need for a sustainable environment and viable energy sources has sparked profound interest in the development of energy storage techniques.<sup>1</sup> While lithium-ion batteries (LIBs) have demonstrated exceptional success in powering portable electronics and electric vehicles, it is imperative to reassess the feasibility of relying exclusively on lithium resources in light of the growing costs and constrained availability.<sup>2–4</sup> Despite its widespread distribution throughout the Earth's crust and sea, lithium is not deemed an abundant element. Furthermore, the majority of the easily accessible global lithium reserves are situated in remote or politically sensitive areas.<sup>5–7</sup> The exponential surge in demand for lithium in energy storage applications is expected to drive up the price of lithium compounds, notwithstanding its inherent attributes of high energy density and long cycle life.

In contrast, sodium boasts nearly limitless availability and ranks as the Earth's 6th most abundant element within its crust. Despite its higher redox potential ( $-2.71$  V *vs.* SHE) and over threefold molar mass when compared to lithium,<sup>8</sup> sodium-ion batteries (SIBs) have emerged as the prime alternative to LIBs for large-scale power storage, while only slightly compromising energy density, as evidenced in Table 1.<sup>9,10</sup> Although SIBs were initially explored alongside LIBs in the mid-1980s, their development was impeded by the successful commercialization of LIBs by Sony in 1990. Nevertheless, in the past decade, researchers have redirected their focus to SIBs due to the escalating demand for extensive energy storage solutions.<sup>11–15</sup>

This review aims to provide an in-depth understanding of the comparable behaviors and distinct electrochemical mechanisms exhibited by  $\text{Na}^+/\text{Li}^+$  ion batteries, focusing specifically on cathode materials commonly employed, including layered transition-metal oxides, polyanionic compounds, and open-frame-work materials. Moreover, we aim to delineate the discrepancies in electrochemical performance between SIBs and LIBs. Additionally, we present a comprehensive overview and discussion of computational studies investigating the differential mobility of  $\text{Na}^+/\text{Li}^+$  ions within solid-state lattices, as well as the utilization of *in situ* and *ex situ* methodologies to unravel the intricate aspects of SIBs. It is worth acknowledging

<sup>a</sup>College of Materials and New Energy, Chongqing University of Science and Technology, Chongqing 401331, China<sup>b</sup>College of Chemical and Biological Engineering, Zhejiang University, Hangzhou 310058, China. E-mail: wanglg@zju.edu.cn<sup>c</sup>MIIT Key Laboratory of Critical Materials Technology for New Energy Conversion and Storage, School of Chemistry and Chemical Engineering, Harbin Institute of Technology, Harbin 150001, China. E-mail: zuopj@hit.edu.cn

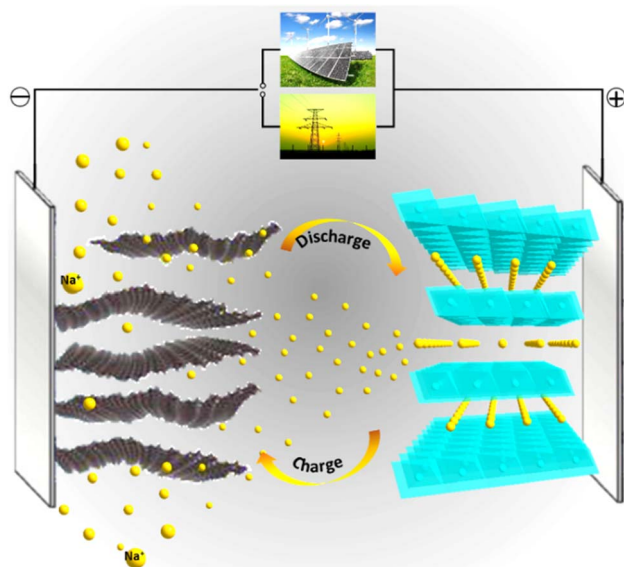
**Table 1** Comparison of physical properties and abundance in the Earth's crust for lithium and sodium<sup>9,10</sup>

| Element   | Li <sup>+</sup>      | Na <sup>+</sup> |
|---|----------------------|-----------------|
| Relative atomic mass/(g mol <sup>-1</sup> )                   | 6.94                 | 23.00           |
| Shannon's ionic radii/Å                                       | 0.76                 | 1.02            |
| <i>E</i> <sup>0</sup> (vs. SHE)/V                             | -3.04                | -2.71           |
| Theoretical capacity of metal electrodes/mA h g <sup>-1</sup> | 3861                 | 1166            |
| Material abundance/ppm  | 20                   | 23 600          |
| Distribution  | 70% in South America | Everywhere      |

the existence of numerous outstanding review articles published in recent years.<sup>16–32</sup> Hence, our focal point lies in differentiating the electrochemical behaviors and elucidating the phase transformation mechanisms unique to sodium-based systems, in contrast to LIBs.

## 2. Cathode materials: a brief introduction

SIBs operate on the fundamental principle known as the “rocking chair” mechanism, which is analogous to that of LIBs. In this mechanism, sodium ions traverse between the cathode (positive electrode) and anode (negative electrode) electrodes through an aprotic electrolyte solution, typically employing organic carbonate ester solvents combined with sodium salts (Fig. 1). The cell architecture, constituent components, and underlying reaction mechanisms of SIBs closely resemble those observed in LIBs. Initially, during the 1980s, the development of SIBs progressed in tandem with the advancements made in lithium-ion battery technology. However, the comparatively lower energy density of SIBs, resulting from their reduced potential, gradually diminished research interest when

**Fig. 1** Schematic illustration of Na-ion batteries.

compared to the commercially prevalent LIBs. In recent times, the escalating demand for large-scale power sources has rekindled researchers' pursuit of sodium-ion battery innovations. Inspired by the achievements of LIBs, cathode materials for SIBs have predominantly been derived from analogues materials utilized in LIBs, encompassing layered structure materials, polyanionic compounds, and other related counterparts.<sup>33–35</sup> In addition, the exploration of Prussian blue analogues as a novel class of cathode materials for SIBs has captivated the attention of numerous researchers, leading to extensive investigations in this area.<sup>36–38</sup> Hence, this review will primarily focus on a comprehensive analysis of these cathode material categories, namely layered structure materials, polyanionic compounds, NASICON compounds, and Prussian blue analogues.

The remarkable commercial success achieved by layered oxides cathodes in LIBs has sparked significant scientific interest in the case of layered NaMO<sub>2</sub> materials (M = Co, Fe, Mn, Ni, *etc.*, or their combinations).<sup>39–46</sup> Particularly, the low or cobalt-free layered materials, including those based on environmentally friendly iron and manganese, have demonstrated exceptional reversible capacity and prolonged cycle life. These contributions augment the promising application potential of layered oxides cathodes for large-scale energy storage systems. Layered structures typically consist of stacked sheets comprising edge-sharing MO<sub>6</sub> octahedra. According to the classification proposed by Delmas *et al.*, Na-layered oxides can be categorized into distinct structures based on the surrounding Na environment, namely O3-type (ABCABC), P2-type (ABBA), O2-type (ABAC), and P3-type (ABBCC) structures, as illustrated in Fig. 2a.<sup>26,32,48</sup> The labels “O” and “P” denote the accommodation of Na<sup>+</sup> ions at octahedral and prismatic sites, respectively. The indicators “3” or “2” signify the number of transition metal layers in a repeating stacking unit, while the prime symbol (') represents the monoclinic distortion phase. It is worth noting that in lithium-containing layered compounds, the smaller ionic size of Li<sup>+</sup> ions prohibits their occupation of trigonal prismatic sites.

Polyanionic compounds have garnered significant attention in the field of LIBs due to their excellent thermal stability and higher redox potential resulting from the inductive effect of the XO<sub>4</sub> or XO<sub>3</sub> polyanion. These advantageous properties have spurred extensive investigations into polyanionic framework compounds, including phosphates,<sup>49–51</sup> fluorophosphates,<sup>52–54</sup> sulfates,<sup>55,56</sup> and other novel polyanionic cathode systems for Na<sup>+</sup> ions.<sup>34,57</sup> In addition, the presence of facile Na<sup>+</sup> diffusion pathways and the tunability of local coordination environments present key benefits for SIBs. The exploration of polyanionic framework compounds for SIBs finds inspiration from their successful implementation in LIBs. However, it is important to note that many Na-based polyanionic cathode materials exhibit unique properties compared to their lithium-ion counterparts. For example, naturally occurring phosphate NaMPO<sub>4</sub> (M = Fe, Mn, Co, *etc.*) adopts the thermodynamically stable maricite structure, which lacks free Na<sup>+</sup> migration pathways and exhibits negligible electrochemical performance, unlike the olivine-structured LiMPO<sub>4</sub>. The latter

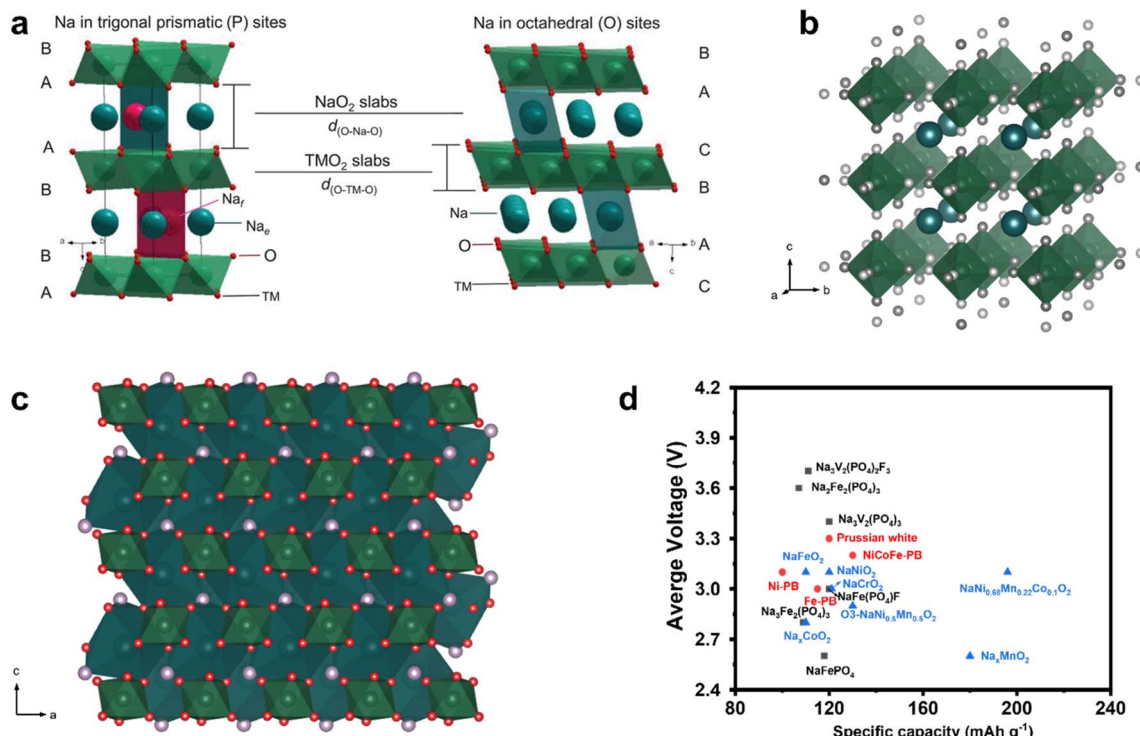


Fig. 2 (a) Crystal structures of (a) O3 and P2-type NaMO<sub>2</sub> (M = transition metal). Reproduced from ref. 47 with permission from AAAS, copyright 2020. (b) Prussian blue, (c) olivine (d) capacity–voltage plot of three representative cathodes for SIBs.

demonstrates one-dimensional lithium transport paths, leading to superior electrochemical performance.<sup>50,58,59</sup> This discrepancy arises from the inverse positioning of transition metal M<sup>2+</sup> ions and alkali metal Na<sup>+</sup> ions in the maricite structure, in contrast to olivine structure materials. Consequently, although various olivine NaMPO<sub>4</sub> cathode materials for SIBs have been reported (Fig. 2c),<sup>50,60,61</sup> most of them necessitate chemical or electrochemical Li/Na exchange methods to be synthesized from LiMPO<sub>4</sub>.

NASICON compounds, characterized by their open 3D frameworks, feature corner-sharing MO<sub>6</sub> octahedra and XO<sub>4</sub> tetrahedra, which create abundant Na<sup>+</sup> diffusion tunnels. Originally recognized for their fast Na<sup>+</sup> ion transport properties,<sup>62</sup> these materials have more recently gained attention as cathode materials. In fact, NASICON phosphate materials were initially explored as hosts for Li intercalation by Padhi *et al.*,<sup>63</sup> utilizing redox couples such as V<sup>4+</sup>/V<sup>3+</sup>, V<sup>3+</sup>/V<sup>2+</sup>, Fe<sup>3+</sup>/Fe<sup>2+</sup>, Ti<sup>4+</sup>/Ti<sup>3+</sup>, Nb<sup>4+</sup>/Nb<sup>3+</sup>, and Nb<sup>5+</sup>/Nb<sup>4+</sup>. For instance, Li<sub>3</sub>V<sub>2</sub>(PO<sub>4</sub>)<sub>3</sub> (P2<sub>1</sub>/n) features a three-dimensional structure consisting of mildly distorted metal octahedra and phosphorus tetrahedra, interconnected through shared apical oxygen atoms to form a (M–O–P–O)<sub>n</sub> bonding framework. One Li(1) ion forms a tetrahedron with four surrounding oxygen atoms, while Li(2) and Li(3) adopt highly distorted tetrahedral environments.<sup>64,65</sup> In contrast, the typical NASICON-type Na<sub>3</sub>V<sub>2</sub>(PO<sub>4</sub>)<sub>3</sub> (R3c) material consists of isolated VO<sub>6</sub> octahedra and PO<sub>4</sub> tetrahedral units interconnected through corner sharing, creating the framework anion [V<sub>2</sub>(PO<sub>4</sub>)<sub>3</sub>]<sup>3-</sup>. One Na<sup>+</sup> ion occupies the M1 (6b) site, while the other two reside in the M2 (18e) site within the interstitial

positions.<sup>49,66</sup> These distinct structural characteristics contribute to the unique physical and electrochemical properties exhibited by NASICON Na-ion compounds, necessitating comprehensive investigations. Additionally, the introduction of fluorine (F) elements into phosphates can form fluorophosphates with higher redox potentials, attributed to the presence of highly electronegative fluorine atoms.<sup>52</sup>

The intercalation and extraction of Na<sup>+</sup> ions in cathode materials generally result in a larger lattice volume expansion or contraction compared to that observed in LIBs due to the larger ionic radius of sodium (1.02 Å) compared to lithium (0.76 Å). As a result, Prussian blue analogues (PBAs) have garnered attention as promising alternative cathode materials for SIBs in comparison to the layered oxides and polyanion structures, owing to their relatively open framework structure (Fig. 2b).<sup>67</sup> This framework provides benefits in terms of volume expansion and structural stability during the insertion and extraction of Na<sup>+</sup> ions.<sup>68–72</sup> An exemplary Prussian blue, K[Fe<sup>III</sup>Fe<sup>II</sup>(CN)<sub>6</sub>]·yH<sub>2</sub>O, (y ≈ 1–5), features a cubic framework (space group *Fm3m*) with alternating Fe(II) and Fe(III) ions occupying the corners of corner-shared octahedra, bridged by linear (C≡N)<sup>-</sup> ligands.<sup>73</sup> This arrangement allows the low-spin Fe(II) ions to bond with C atoms, while the high-spin Fe(III) ions bond with N atoms. Moreover, the cyano ligands expose the faces of the elementary cubes, providing pathways for Na<sup>+</sup> ions to travel between the half-filled body-center positions.<sup>74</sup> Although PBAs can accommodate reversible intercalation of both lithium and sodium ions, their behavior during the insertion and extraction process differs, which will be discussed later.<sup>75,76</sup>

### 3. Energy storage mechanism in Na-ion batteries

The intercalation/de-intercalation mechanisms of battery materials have a direct impact on their physical and electrochemical performance. In the case of cathode materials for SIBs, the mechanisms involved in sodium insertion and extraction are often more intricate compared to their LIBs counterparts. This complexity arises from multiple factors, including the larger radius of sodium ions, the presence of distinct ion diffusion pathways and barriers, and voltage variations, among others. Gaining a comprehensive understanding of the fundamental energy storage and phase transformation mechanisms is paramount for the development of advanced cathode materials tailored specifically for SIBs. Therefore, in this review, we provide a detailed summary of the electrochemical reaction mechanisms of cathode materials for SIBs, drawing comparisons with analogous systems employed in LIBs.

#### 3.1. Layered oxides cathodes

**3.1.1. NaCoO<sub>2</sub>.** In the 1980s, layered cobaltates garnered renewed scientific interest due to reports of exceptional thermoelectric properties exhibited by the NaCo<sub>2</sub>O<sub>4</sub> crystal material, as well as the discovery of superconductivity in the P2-Na<sub>0.35</sub>-CoO<sub>2</sub>·1.3H<sub>2</sub>O hydrated compound. As a result, researchers directed their efforts towards studying the structure and physical properties of materials within this system, which is characterized by a complex phase diagram with numerous phases possessing similar sodium concentrations. The vast body of research on this material family encompasses over six hundred papers, demonstrating the extensive exploration within the Na<sub>x</sub>CoO<sub>2</sub> system. The phase diagram of P2-Na<sub>x</sub>CoO<sub>2</sub> has been extensively investigated for  $x \geq 0.5$  using *in situ* X-ray diffraction technique in conjunction with electrochemical processes. These studies have revealed a sequence of single-phase or two-phase domains during the electrochemical processes.<sup>77</sup> Notably, narrow ranges of sodium composition ( $0.5 \leq x \leq 1$ ) have been identified, demonstrating distinctive Na<sup>+</sup>/vacancy ordering at room temperature. The Na<sub>x</sub>CoO<sub>2</sub> phases exhibit notable voltage plateaus, which sharply contrast with the solid-state delithiation/lithiation process observed in Li<sub>x</sub>CoO<sub>2</sub>.<sup>78</sup> The dissimilar phase transitions and biphasic behavior between Na<sub>x</sub>CoO<sub>2</sub> and Li<sub>x</sub>CoO<sub>2</sub> can be attributed to the presence of similar charge ordering (electron–electron interaction). The role of sodium ions in these distinctions has been thoroughly investigated, and the content and ordering of Na<sup>+</sup> ions have been carefully analyzed to understand their influence on the phase transitions.<sup>28</sup> In the case of the O3-type phase, only octahedral sites exist between CoO<sub>2</sub> layers, while the P2-Na<sub>x</sub>-CoO<sub>2</sub> phase presents two distinct prismatic sites. The intricate Na ordering within the crystal plane stems from the interplay of repulsive interactions, including sodium–sodium and sodium–cobalt interactions that are specific to the P2 phase.

**3.1.2. Na<sub>x</sub>MnO<sub>2</sub>.** The acquisition of the layered LiMnO<sub>2</sub> phase is solely achievable through Li/Na exchange from its Na

phase. However, due to the high mobility of Mn<sup>2+</sup>, the LiMnO<sub>2</sub> phase tends to undergo a transformation into spinel following the initial charge or discharge process.<sup>79</sup> This occurrence stands in stark contrast to the behavior of NaMnO<sub>2</sub> material in SIBs. NaMnO<sub>2</sub> exists in two primary phases: the low-temperature  $\alpha$ -NaMnO<sub>2</sub> with an O'3 layered structure, and high-temperature orthorhombic  $\beta$ -NaMnO<sub>2</sub>. Similar to O3-LiCoO<sub>2</sub>, the crystal structure of  $\alpha$ -NaMnO<sub>2</sub> also exhibits a layered configuration, rendering it stable during the reversible insertion and extraction of Na<sup>+</sup> ions. The  $\alpha$ -NaMnO<sub>2</sub> phase exhibits a distorted version of the  $\alpha$ -NaFeO<sub>2</sub> structure, resulting from the pronounced distortion of MnO<sub>6</sub> octahedra due to the Jahn–Teller effect. The Jahn–Teller effect is a lattice distortion phenomenon that breaks the local crystal symmetry, prompting a structural rearrangement through certain bond length distortions that lowers the energy of a system.<sup>80</sup> For Na<sub>x</sub>MnO<sub>2</sub>, the Jahn–Teller effect can induce lattice distortions and irreversible phase transition that affect the electrochemical behavior of Na<sub>x</sub>MnO<sub>2</sub>. Such distortions can lead to lower reversible capacity and cycling performance of Na<sub>x</sub>MnO<sub>2</sub> cathode materials.<sup>81</sup> In contrast,  $\beta$ -NaMnO<sub>2</sub> differs from the conventionally observed NaMO<sub>2</sub> type structures, as it comprises MnO<sub>2</sub> sheets consisting of a double stack of edge-sharing MnO<sub>6</sub> octahedra. Both  $\alpha$ - and  $\beta$ -NaMnO<sub>2</sub> have undergone electrochemical testing as positive electrode materials since 1985.<sup>82</sup> Among the two,  $\alpha$ -NaMnO<sub>2</sub> material has been extensively investigated due to its superior chemical stability.<sup>83</sup> It is proved that 0.85 Na can be de-intercalated with a reversible intercalation of 0.8 Na, as shown in Table 2.<sup>86</sup> Notably, the sequence of phase transformation during charge and discharge is dissimilar, consistent with the strong first-order character of the phase transformations—a typical characteristic of reactions involving significant phase transformation barriers. Consequently, nucleation may not occur symmetrically when the two phases on each side of the transition are distinct.<sup>109</sup> The precise factors contributing to the pronounced transitions in  $\alpha$ -NaMnO<sub>2</sub> remain unclear at present. Moreover, the charge–discharge curves distinctly exhibit prominent features, such as strong voltage steps and plateau, indicating phase transitions upon desodiation. This phenomenon suggests a larger hysteresis compared to the lithium de-intercalation/intercalation observed in LIBs. These multiple voltage plateaus and phase transformation features resemble the behavior observed in NaCoO<sub>2</sub>, as mentioned earlier, but are in contrast to their lithium-ion intercalation systems.

**3.1.3. NaVO<sub>2</sub>.** Due to their intriguing physical properties arising from the coexistence of V<sup>4+</sup> and V<sup>3+</sup> ions in the rutile and corundum structures, respectively, vanadium oxides (V<sub>2</sub>O<sub>3</sub> and VO<sub>2</sub>) garnered significant attention in the 1970s.<sup>110,111</sup> Researchers have explored the possibility of developing a new family of highly correlated electron materials by incorporating these ions into a layered structure.<sup>90</sup> However, the facile reducibility of V<sup>3+</sup> ions posed challenges in the investigation of Na<sub>x</sub>VO<sub>2</sub> materials. Initially, substantial efforts were dedicated to studying the O3-NaVO<sub>2</sub> phase, but its synthesis often yielded impurities. In 2008, O3-NaVO<sub>2</sub> was successfully synthesized by a solid-state reaction method, and a comprehensive structural

Table 2 The mechanism comparison of selected cathode materials for LIBs and SIBs

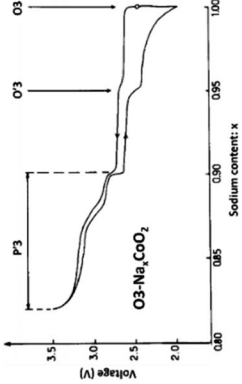
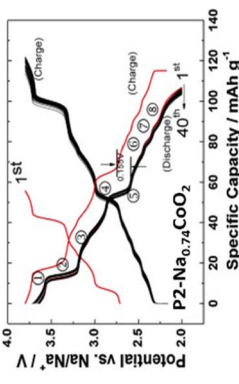
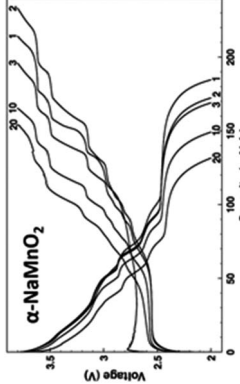
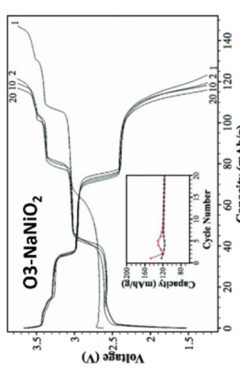
| Materials                                  | Charge-discharge Curves   | Mechanism  | Li-contained materials   |
|--|---|--|--|
| $\text{Na}_x\text{CoO}_2$ (ref. 84 and 85) |  <p>Reproduced from ref. 84 with permission from Elsevier, copyright 1981</p>                      | O3-O'3-P'3   | A typical solid-state reaction as the layered structure material             |
| $\text{Na}_x\text{MnO}_2$ (ref. 86 and 87) |  <p>Reproduced from ref. 85 with permission from Elsevier, copyright 2013</p>                      | A series of two-phase transition and solid-state reaction  | —  |
| $\text{Na}_x\text{MnO}_2$ (ref. 86 and 87) |  <p>Reproduced from ref. 86 with permission from the Electrochemical Society, copyright 2011</p>  | $\text{Na}_{0.95}\text{MnO}_2$ (O3)- $\text{Na}_{0.7}\text{MnO}_2$ (O'3) and a series of two-phase transition and monophasic processes | Phase transition into spinel on electrochemical cycling for $\text{LiMnO}_2$ |
| $\text{NaNiO}_2$ (ref. 88)                 |  <p>Reproduced from ref. 88 with permission from the Electrochemical Society, copyright 2012</p> | O'3-P'3-P''3-O'3-O'''3   | Hexagonal-monoclinic-hexagonal <sup>189</sup>                                |

Table 2 (Contd.)

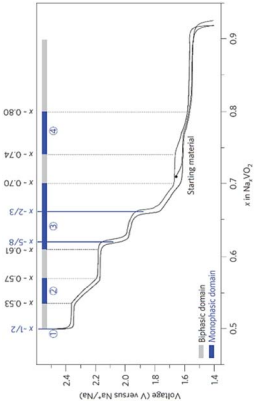
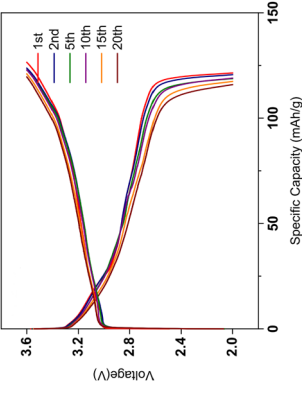
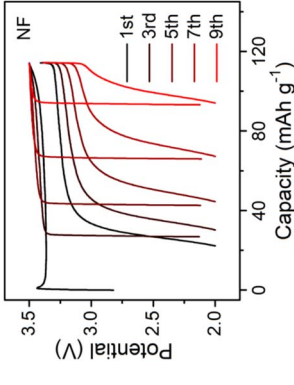
| Materials                          | Charge-discharge Curves   | Mechanism  | Li-contained materials   |
|------------------------------------|---|--|--|
| $\text{Na}_x\text{VO}_2$ (ref. 90) |  <p>Reproduced from ref. 90 with permission from Springer Nature, copyright 2013</p> | Four biphasic and three monophasic processes as labeled in the charge-discharge curves     | As an anode with a short two-phase evolution process <sup>91</sup> |
| $\text{NaCrO}_2$ (ref. 92 and 93)  |  <p>Reproduced from ref. 92 with permission from Wiley-VCH GmbH, copyright 2023</p>  | $\text{O}_3(\text{hexagonal})\text{-O}_3(\text{monoclinic})\text{-P}_3(\text{monoclinic})$ | Electrochemical inactive for $\text{LiCrO}_2$                      |
| $\text{NaFeO}_2$ (ref. 94 and 95)  |  <p>Reproduced from ref. 94 with permission from Wiley-VCH GmbH, copyright 2023</p> | Two-phase conversion mechanism   | Electrochemical inactive for $\text{LiFeO}_2$                      |

Table 2 (Contd.)

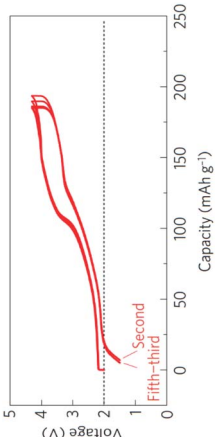
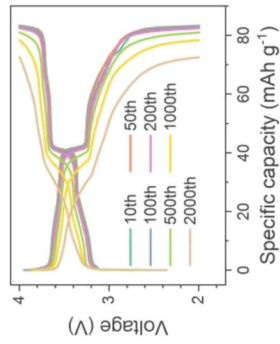
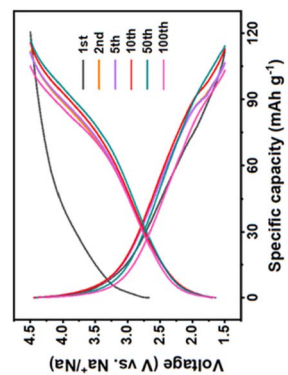
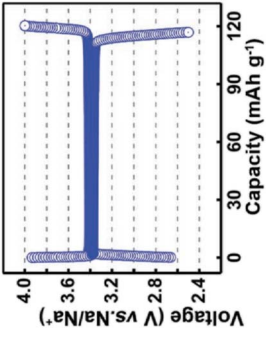
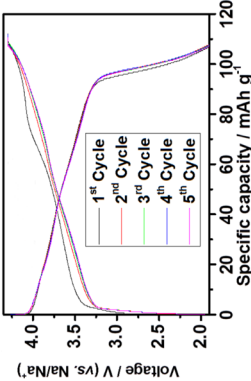
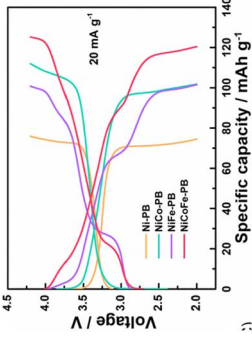
| Materials  | Charge-discharge Curves  | Mechanism  | Li-contained materials  |
|--|--|--|---|
| $\text{Na}_x[\text{Fe}_{1/2}\text{Mn}_{1/2}]\text{O}_2$ (ref. 96)      |  <p>Reproduced from ref. 96 with permission from Springer Nature, copyright 2012</p>  | P2-OP4 compared to O3-Na <sub>2/3</sub> [Fe <sub>1/2</sub> Mn <sub>1/2</sub> ] <sub>2</sub> O <sub>2</sub> (O3-P3-OP2)       | —   |
| $\text{Na}_x\text{Ni}_{1/3}\text{Mn}_{2/3}\text{O}_2$ (ref. 97 and 98) |  <p>Reproduced from ref. 98 with permission from Wiley-VCH GmbH, copyright 2021</p>   | P2-type monophase-P2-type + O2-type biphasic-O2-type monophase   | Both phase transition and solid state process with a spinel phase formation <sup>99</sup> |
| $\text{NaFePO}_4$ (ref. 100 and 101)                                   |  <p>Reproduced from ref. 100 with permission from Wiley-VCH GmbH, copyright 2023</p> | Maricite $\text{NaFePO}_4 \leftrightarrow \text{Na}_{0.7}\text{FePO}_4$ (intermediate phase) $\leftrightarrow \text{FePO}_4$ | A classical two-phase reaction mechanism for $\text{LiFePO}_4$                            |

Table 2 (Contd.)

| Materials   | Charge-discharge Curves  | Mechanism   | Li-contained materials  |
|---|--|---|---|
| $\text{Na}_3\text{V}_2(\text{PO}_4)_3$ (ref. 102–104) |  <p>Reproduced from ref. 104 with permission from Wiley-VCH GmbH, copyright 2021</p>  | A typical two-phase reaction (>3V vs. Na <sup>+</sup> /Na) $\text{Na}_3\text{V}_2(\text{PO}_4)_3 \leftrightarrow \text{NaV}_2(\text{PO}_4)_3$ | $\text{Li}_x\text{V}_2(\text{PO}_4)_3$ with three two-phase transitions between $x = 2.5$ , 2.0, and 1.0 (ref. 105) |
| $\text{Na}_2\text{Fe}_2(\text{SO}_4)_3$ (ref. 106)    |  <p>Reproduced from ref. 106 with permission from Wiley-VCH GmbH, copyright 2018</p>  | A single-phase homogeneous reaction with some irreversible structural transformation during 1st cycle   | The similar electrochemical behavior to $\text{Na}_2\text{Fe}(\text{SO}_4)_2$                                       |
| Prussian blue analogues <sup>107</sup>                |  <p>Reproduced from ref. 107 with permission from Wiley-VCH GmbH, copyright 2021</p> | Two or three-phase transitions  | No phase transitions with a solid-state mechanism <sup>108</sup>  |

study was reported.<sup>112</sup> Subsequently, an *in situ* X-ray diffraction experiment during the charge and discharge process provided a phase diagram for the P2-Na<sub>x</sub>VO<sub>2</sub> system, revealing four primary single phases within 0.5 < x < 0.9 range.<sup>90</sup> Analogous to the P2-Na<sub>x</sub>CoO<sub>2</sub> system, the curves (Table 2) displayed multiple potential plateaus, characteristic of biphasic systems and continuous solid solutions. Notably, the charge–discharge curves exhibited distinct compositions with special structures at 2.40 V, 2.07 V and 1.84 V for P2-Na<sub>1/2</sub>VO<sub>2</sub>, P2-Na<sub>5/8</sub>VO<sub>2</sub> and P2-Na<sub>2/3</sub>VO<sub>2</sub>, respectively. Further investigations encompassed both Na<sub>2.46</sub>V<sub>6</sub>O<sub>16</sub> (NVO) and Li<sub>2.55</sub>V<sub>6</sub>O<sub>16</sub> cathodes, with primary focus on the structural evolution using *operando* synchrotron X-ray diffraction.<sup>113</sup> During cycling between 4.0 and 1.6 V, NVO demonstrated reversible Na-ion occupation in two different crystallographic sites, α and β. However, discharging to 1.0 V led to additional Na-ions occupation in interstitial sites, inducing irreversible structural changes and a subsequent capacity decrease. Furthermore, the incorporation of a minor Li<sup>+</sup> into the crystal structure contributed to the stabilization of the layered structure, effectively mitigating irreversible structural damage.

**3.1.4. NaNiO<sub>2</sub>.** Despite extensive research on LiNiO<sub>2</sub> as high-capacity positive electrode material over the years, achieving a perfect stoichiometric LiNiO<sub>2</sub> phase experimentally has proven to be a rare accomplishment. Instead, the more commonly obtained phase is an off-stoichiometric Li<sub>1-x</sub>Ni<sub>1+x</sub>O<sub>2</sub>, where Ni<sup>2+</sup> partially occupies the lithium site.<sup>114</sup> This occurrence is attributed to the charge disproportionation reaction Ni<sup>3+</sup> → Ni<sup>2+</sup> + Ni<sup>4+</sup> or the Ni<sup>3+</sup> Jahn–Teller effect in the NiO<sub>2</sub> layer, leading to distortion of the LiO<sub>6</sub> octahedron.<sup>115,116</sup> Regrettably, the presence of Ni<sup>2+</sup> in the lithium layers significantly compromises the electrochemical performance of LiNiO<sub>2</sub> compounds. In contrast, NaNiO<sub>2</sub> materials exhibit a stronger propensity for synthesis in a layered structure due to the larger difference in ionic radius between the transition metal and sodium. Furthermore, the larger Na<sup>+</sup> ion effectively impedes charge disproportionation and Ni<sup>3+</sup> Jahn–Teller distortions. The pioneering investigation of NaNiO<sub>2</sub> in both electrochemical and structural aspects dates back 1982, wherein the analysis revealed multiple phase transitions mechanism occurring up to approximately 3.7 V.<sup>117</sup> These transitions correspond to the de-intercalation of only 0.2 Na ions during the initial charge process. Upon electrochemical cycling of the NaNiO<sub>2</sub> compound, multiple plateaus are observed, attributed to complex phase transitions, structural distortion, or Na redistribution in the interlayer.<sup>118</sup> *In situ* XRD experiments have conclusively demonstrated several phase transitions from O'3 → P'3 → P''3 → O''3 → O'''3.<sup>119</sup> The composition of the O'''3-phase corresponds to Na<sub>0.83</sub>NiO<sub>2</sub>, representing the closest composition to the fully sodiated phase during the discharge process to date. Nevertheless, even after the initial discharge process, a fully sodiated phase (NiO<sub>2</sub> composition) remains elusive, and the underlying reasons for this phenomenon have not yet been definitively elucidated.

**3.1.5. NaFeO<sub>2</sub>.** The extensive research on LiFeO<sub>2</sub> has primarily focused on its layered analogue, LiCoO<sub>2</sub>, the corrugated phase, and compounds based on ramsdellite and hollandite structures.<sup>120</sup> Unfortunately, none of these materials have

exhibited the required structural stability or prolonged cycling capability when used solely as electrode materials.<sup>121</sup> Furthermore, there have been no reports of direct synthesis of LiFeO<sub>2</sub> with O3-type layered structures through high temperature solid-state reaction to date. This occurrence can be attributed to the similarity in ionic radii between Li<sup>+</sup> and Fe<sup>3+</sup>, leading to the facile formation of a cation-disordered rock-salt phase during solid-state reactions at elevated temperatures, a phenomenon analogous to that observed in LiNiO<sub>2</sub> as mentioned above. Although successful synthesis of a single phase of LiFeO<sub>2</sub> was achieved *via* a mixed-alkaline hydrothermal method, the resulting material proved as electrochemically inactive.<sup>122</sup> In contrast, NaFeO<sub>2</sub> stands as a prominent example of an O3-type layered structure and can be readily prepared through conventional solid-state reactions.<sup>123</sup> In 1994, during the charge process, a monoclinic structure distorted phase (O'3) with a space group C2/m was observed in NaFeO<sub>2</sub>.<sup>124</sup> This structural distortion at the fully charged state was attributed to the loss of Na ions and Jahn–Teller effect of Fe<sup>4+</sup>. To assess the electrochemical reversibility of sodium extraction/insertion processes for the single phase of O3-type NaFeO<sub>2</sub>, experiments were conducted in aprotic sodium cells. The extent of reversibility was found to be significantly influenced by the cut-off voltage conditions applied during the charging process, as detailed in Table 2. While the charging capacity exhibited an increase with the cut-off voltage, the reversible capacity declined when charged beyond 3.5 V. Notably, up to approximately 70% of Na was extracted from O3-type NaFeO<sub>2</sub> until oxidation reached 4.5 V. However, the material's activity was severely compromised when excessive Na ion extraction occurred, rendering it nearly electrochemically inactive. Furthermore, *in situ* advanced synchrotron XRD on NaFeO<sub>2</sub> revealed a new hexagonal phase (O''3) at the charged state. This discovered phase was identified as a sodium-deficient topotactic phase and demonstrated reversibility when sodium was reinserted into the material after discharge.<sup>125</sup>

**3.1.6. NaCrO<sub>2</sub>.** Cathode materials based on chromium (Cr) have garnered considerable interest due to their multiple electron transfers, offering the prospect of higher energy storage capacities. However, initial investigations of LiCrO<sub>2</sub>, which shares the same structure as LiCoO<sub>2</sub>, revealed limited reversible lithium intercalation.<sup>126</sup> This was attributed to the tendency of the charged state Cr<sup>4+</sup> ions to disproportionate into Cr<sup>6+</sup> and Cr<sup>3+</sup>, adopting stable electronic configurations of d<sup>0</sup> and d<sup>3</sup>, respectively. Consequently, during cycling, Cr ions readily and reversibly migrated into the octahedral lithium sites, resulting in a notable irreversible capacity.<sup>127,128</sup> The atomic-level crystal structure instability of LiCrO<sub>2</sub> was directly visualized using high-angle-annular-dark-field transmission electron microscopy (HAADF-TEM).<sup>129</sup> Comparing the structures of LiCrO<sub>2</sub> and NaCrO<sub>2</sub> revealed that the interstitial tetrahedron in LiCrO<sub>2</sub>, which shares faces with CrO<sub>6</sub> octahedra, aligns more favorably with the tetrahedron CrO<sub>4</sub><sup>2-</sup> compared to NaCrO<sub>2</sub>. This structural mismatch in NaCrO<sub>2</sub> hinders the occupation of the interstitial tetrahedron by Cr<sup>6+</sup> ions, preventing the observed irreversible migration of Cr ions in LiCrO<sub>2</sub>.<sup>93,130</sup> Consequently, in Na-containing systems, the small Cr<sup>6+</sup> ions encounter difficulties in migrating into the relatively large tetrahedral sites

within Na layers, leading to the energetic stabilization of  $\text{Cr}^{6+}$ ,  $\text{Cr}^{4+}$  in  $\text{Na}_x\text{CrO}_2$ .<sup>93</sup> In-depth structural investigations of  $\text{NaCrO}_2$  during intercalation/extraction were conducted using *ex situ* and *in situ* XRD techniques. These studies have elucidated a notable transformation sequence within  $\text{O}3\text{-NaCrO}_2$ , transitioning from its initial  $\text{O}3$  type to an  $\text{O}'3$  structure, and subsequently to  $\text{P}'3$  during electrochemical desodiation.<sup>131,132</sup> Deep charging prompts  $\text{O}3\text{-NaCrO}_2$  to transition from the crystalline  $\text{P}'3\text{-Na}_x\text{CrO}_3$  phase to a disordered phase, characterized by Cr migration into interlayer spaces. XANES analysis confirms the presence of  $\text{Cr}(\text{vi})$ , resulting from the disproportionation of  $\text{Cr}(\text{iv})$ . Additionally, PDF analysis indicates the positioning of Cr on tetrahedral sites. This Cr migration impedes Na-ion reinsertion, leading to irreversibility in the electrochemical process. *Operando* PDF analysis further reveals that despite expectations of solid solution behavior, a first-order transition is observed, with disordering occurring at higher states of charge, up to 3.8 V.<sup>133</sup> Notably, when a reversible phase transition occurs at 3.8 V, a distinct electron paramagnetic resonance (EPR) spectral signature is unequivocally identified, attributed to the dissolution of  $\text{Cr}^{5+}$  ions during the surface reconstruction process.<sup>134</sup>

### 3.2. Polyanionic compounds

Olivine-type  $\text{LiFePO}_4$  has garnered significant attention as a highly competitive material for LIBs used in electric vehicles, owing to its exceptional thermal stability, which was first reported by Goodenough in 1997.<sup>135</sup> The superior thermal safety of  $\text{LiMPO}_4$  ( $\text{M} = \text{Fe}, \text{Mn}, \text{Co}$ , *et al.*) is attributed to the remarkably strong covalent bonds (P–O) present in the tetrahedral ( $\text{PO}_4$ ) structure. In the case of olivine  $\text{LiFePO}_4$ , lithium ions are believed to diffuse along the (010) direction, following a one-dimensional pathway, and involve a two-phase diffusion process.<sup>136,137</sup> On the other hand,  $\text{NaFePO}_4$ , in contrast to its celebrated lithium counterpart, crystallizes in the more thermodynamically stable maricite structure, which unfortunately lacks free pathways for Na ions transportation.<sup>138–140</sup> Currently, it is feasible to prepare electrochemically active olivine-type  $\text{NaFePO}_4$  through a low-temperature Li/Na ion exchange process from  $\text{LiFePO}_4$  while retaining the olivine-type structural features.<sup>141</sup> However, the charge–discharge curves of  $\text{NaFePO}_4$  in SIBs exhibit a distinct intermediate phase of  $\text{Na}_{0.7}\text{FePO}_4$  (Table 2).<sup>101</sup> Nevertheless, the electrochemical kinetics of  $\text{NaFePO}_4$  are notably slower compared to those of  $\text{LiFePO}_4$ , mainly due to the substantial volume change occurring between the reduced and oxidized phases. Furthermore, the absence of a metastable phase and solid-solution behavior contributes to the relatively sluggish electrochemical kinetics of  $\text{NaFePO}_4$ , while  $\text{LiFePO}_4$  benefits from the presence of a solid solution phase, accounting for its excellent kinetics in LIBs.<sup>142,143</sup>

NASICON compounds, known for their open 3D framework, have been extensively explored as solid electrolytes and as promising host materials for  $\text{Li}^+$  and  $\text{Na}^+$  ions.<sup>62</sup> Among these compounds,  $\text{Li}_3\text{V}_2(\text{PO}_4)_3$  adopts a thermodynamically stable monoclinic phase, which distinguishes it from the

rhombohedral or NASICON form. The NASICON  $\text{Li}_3\text{V}_2(\text{PO}_4)_3$  is commonly obtained through ion exchange from its sodium analog,  $\text{Na}_3\text{V}_2(\text{PO}_4)_3$ , and undergoes a distinctive two-phase transformation process between  $\text{Li}_3\text{V}_2(\text{PO}_4)_3$  and  $\text{LiV}_2(\text{PO}_4)_3$ .<sup>144</sup> Notably,  $\text{Na}_3\text{V}_2(\text{PO}_4)_3$  with its NASICON structure has gained attention due to its remarkable thermal stability in the charged state, exhibiting a remarkably flat voltage profile with a prolonged plateau at around 3.4 V vs.  $\text{Na}^+/\text{Na}$ , akin to the behavior observed in  $\text{LiFePO}_4$  vs.  $\text{Li}^+/\text{Li}$ .<sup>66,104</sup> This suggests an extraction/insertion of approximately two Na ions per formula unit during the process (as presented in Table 2). In-depth investigations have revealed the coexistence of two distinct Na sites, namely 6b and 18e, each exhibiting different coordination environments within  $\text{Na}_3\text{V}_2(\text{PO}_4)_3$ . However, it is noteworthy that only Na ions occupying 18e sites can be effectively extracted from the lattice, leading to the formation of the charged state  $\text{NaV}_2(\text{PO}_4)_3$ .<sup>145,146</sup> Electrochemical cycling of the  $\text{Na}_3\text{V}_2(\text{PO}_4)_3$  cathode involves a one-site Na extraction/insertion process, resulting in the characteristic two-phase transformation between the discharged state of  $\text{Na}_3\text{V}_2(\text{PO}_4)_3$  and the charged state of  $\text{NaV}_2(\text{PO}_4)_3$ . Interestingly, even upon charging the voltage up to 4.5 V (vs.  $\text{Na}^+/\text{Na}$ ), a fraction of Na ions remains unextracted from the structure through the electrochemical method.

Various hydrated sulfates, including polymorphs of  $\text{Na}_2\text{-Fe}(\text{SO}_4)_2$ ,<sup>147,148</sup>  $\text{Na}_2\text{FeM}(\text{SO}_4)_3$  ( $\text{M} = \text{Fe}, \text{Mn}, \text{Ni}$ ),<sup>56</sup> and  $\text{Na}_{2+2\delta}\text{Fe}_{2-\delta}(\text{SO}_4)_3$ ,<sup>149</sup> along with their dehydrated derivatives, have demonstrated notable electrochemical activity.  $\text{Na}_2\text{Fe}_2(\text{-SO}_4)_3@C@GO$  was synthesized by a straightforward freeze-drying method, achieving a discharge capacity of  $107.9 \text{ mA h g}^{-1}$  at a rate of 0.1C, and maintains over 90% capacity retention at a higher rate of 0.2C even after 300 cycles. *In situ* synchrotron powder diffraction reveals minimal volume change during cycling, which is crucial for its excellent cyclability. The voltage profile, as presented in Table 2, showcases a continuous sloping trend across the entire range of Na composition, indicating a single-phase (solid-solution) electrochemical reaction mechanism with minimal volume change for  $\text{Na}_2\text{Fe}_2(\text{SO}_4)_3$ . This characteristic is highly promising for potential applications in advanced SIBs.<sup>106</sup>

Fluorosulfates represent an alternative class of sulfates employed in SIBs. Their open framework exhibits a pronounced inductive effect, leading to a significant increase in potential, up to 0.8 V higher than their phosphate counterparts, thus offering distinct advantages. However, it is essential to note that fluorosulfates are highly sensitive to moisture, necessitating the use of a non-aqueous medium for their synthesis. This requirement has led to the discovery of a corner-shared  $\text{NaFeSO}_4\text{F}$  framework.<sup>150,151</sup> Nevertheless, it is crucial to consider the distinctive ion conduction behavior exhibited by  $\text{NaFeSO}_4\text{F}$ , where it functions as an effectively 1D ion conductor, in stark contrast to  $\text{LiFeSO}_4\text{F}$ , which features 3D  $\text{Li}^+$  ion migration pathways.<sup>152</sup> The limited ion mobility of  $\text{NaFeSO}_4\text{F}$ , combined with a substantial volume change during redox processes, contributes to its comparatively poorer electrochemical properties when compared to its lithium-based counterpart. Although the  $\text{NaFeSO}_4\text{F}$  cathode materials exhibited satisfactory electrochemical activity and remarkable redox potential of

approximately 3.7 V, their intricate synthesis process renders the practical application.<sup>153</sup>

### 3.3. Prussian blue analogues (PBAs)

PBAs are characterized by the general chemical formula of  $\text{Na}_{2-x}\text{M}_A[\text{M}_B(\text{CN})_6]_{1-y} \cdot \square_y \cdot z\text{H}_2\text{O}$ , wherein different transition metals ( $\text{M}_A$  and  $\text{M}_B$ ) can be incorporated, and the hexacyanometallate vacancies ( $\square_y$ ) are incorporated into the  $[\text{M}_B(\text{CN})_6]^{4-}$  moieties. Among PBAs, the hexacyanoferrates ( $\text{M}_B = \text{Fe}$ ) have gained considerable popularity in SIBs owing to their cost-effectiveness and facile synthesis.<sup>154–156</sup> In 2012, Goodenough *et al.* introduced the  $\text{KMFe}(\text{CN})_6$  family ( $\text{M} = \text{Mn}, \text{Fe}, \text{Co}, \text{Zn}, \text{Ni}$ ) as promising cathode materials for SIBs.<sup>67</sup> Notably, the charge–discharge curves of these materials exhibit two voltage plateaus at 3.5 V and 2.8 V, respectively. The lower potential plateaus are associated with the high-spin  $\text{Fe}^{3+}/\text{Fe}^{2+}$  redox couple bonded to N atoms, while the higher voltage plateaus correspond to the low-spin  $\text{Fe}^{3+}/\text{Fe}^{2+}$  redox couple bonded to C atoms. Another significant PBA-based cathode material of interest is “Prussian white”, predominantly composed of  $\text{Fe}(\text{II})$  ions, balanced by a high sodium content within the  $\text{Na}_{2-x}\text{Fe}[\text{Fe}(\text{CN})_6]$  framework. A noteworthy contribution includes the synthesis of a novel, air-stable sodium iron hexacyanoferrate ( $\text{R-Na}_{1.92}\text{Fe}[\text{Fe}(\text{CN})_6]$ ) with a rhombohedral structure, accompanied by a comprehensive elucidation of the electrochemical reaction mechanism during cycling.<sup>157</sup> Highly crystalline  $\text{Na}_{2-x}\text{FeFe}(\text{CN})_6$  microcubes, synthesized *via* a scalable co-precipitation method, demonstrated a stable rhombohedral structure. *In situ* synchrotron powder X-ray diffraction (PXRD) unveiled three distinct phase transitions – rhombohedral, cubic, and tetragonal structures-occurring during  $\text{Na}^+$  intercalation/deintercalation processes. Thanks to its structural stability,  $\text{Na}_{1.73}\text{Fe}[\text{Fe}(\text{CN})_6] \cdot 3.8\text{H}_2\text{O}$  showcased a high initial coulombic efficiency of 97.4%. Furthermore, it exhibited a capacity retention of 71% after 500 cycles, with a capacity of  $70 \text{ mA h g}^{-1}$  at a high current density of  $2000 \text{ mA h g}^{-1}$ .<sup>158</sup> This underscores the promising potential of this material for high-performance SIBs.

## 4. Modification strategies and their effect on electrochemical properties

The practical utilization of most current cathode materials for SIBs often results in lower-than-expected capacities. To overcome this challenge and unlock the full potential of most cathode materials, concerted efforts are required to delve deeper into the intricate intercalation and deintercalation processes of sodium ions within the structure. By gaining a comprehensive understanding of these fundamental mechanisms, researchers can devise targeted strategies to enhance the electrochemical performance of cathode materials, ultimately leading to the development of more efficient and high-performance SIBs. To this end, the fundamental electrochemical behaviors of these cathode materials are summarized in this section.

### 4.1. $\text{Na}_x\text{CoO}_2$

Both O3-type and P2-type layered  $\text{Na}_x\text{CoO}_2$  materials can be easily synthesized and demonstrate excellent reversibility in the battery system. Furthermore, the P3-type  $\text{Na}_x\text{CoO}_2$  ( $x \approx 0.62$ ) can be produced at a low temperature, characterized by distorted monoclinic phase at room temperature.<sup>159</sup> Notably, these materials demonstrate significant reversible capacities, with the O3-type phase achieving  $\sim 140 \text{ mA h g}^{-1}$ , the P3-type phase achieving  $\sim 130 \text{ mA h g}^{-1}$ , and the P2-type phase achieving  $120 \text{ mA h g}^{-1}$ . Table 2 presents the corresponding electrochemical reversibility of sodium extraction/insertion processes for selected O3-type layered materials. The pure  $\text{Na}_{0.71}\text{CoO}_2$  cathode materials were successfully synthesized using the solid-state reaction route. This  $\text{Na}_{0.71}\text{CoO}_2$  materials demonstrated a specific capacity of  $70.4 \text{ mA h g}^{-1}$  within a voltage range of 2.0 to 3.5 V at 0.08C, and achieved a coulombic efficiency of 90% in the initial cycle. The voltage profile revealed multiple voltage plateaus, primarily attributed to the slight reordering of sodium ions within the layers of the material. Furthermore, the CV test results of the prepared  $\text{Na}_{0.71}\text{CoO}_2$  indicated the presence of eight couples of peaks during cathodic and anodic sweeps, which correspond closely to the voltage profile observed during the charge–discharge process.<sup>160</sup>  $\text{Na}_{0.60}\text{Ca}_{0.07}\text{CoO}_2$  cathode materials were synthesized through the substitution of  $\text{Ca}^{2+}$  for  $\text{Na}^+$  using a solid-state reaction method. The doping of  $\text{Ca}^{2+}$  did not alter the P2-phase of  $\text{Na}_{0.73}\text{CoO}_2$ . The  $\text{Ca}^{2+}$  ions, which are doped and located between  $\text{CoO}_6$  slabs, influence the phase transition behaviors during the charge–discharge process. This has significantly enhanced the cycle stability of the cathode material. During the 60 charge–discharge cycles, the capacity decay per cycle for the  $\text{Ca}^{2+}$ -doped  $\text{Na}_{0.60}\text{Ca}_{0.07}\text{CoO}_2$  cathode materials is  $0.06 \text{ mA h g}^{-1}$ , while the  $\text{Na}_{0.73}\text{CoO}_2$  material without  $\text{Ca}^{2+}$  doping experiences a decay of  $0.56 \text{ mA h g}^{-1}$  per cycle.<sup>161</sup>

### 4.2. $\text{Na}_x\text{CrO}_2$

The electrochemistry of  $\text{Na}_x\text{CrO}_2$  was initially investigated in 1982, revealing only limited reversibility with a cycling capacity of  $0.15 \text{ Na}$ .<sup>162</sup> However, upon reevaluation, it was observed that the material could achieve an approximate discharge capacity of  $120 \text{ mA h g}^{-1}$ , corresponding to  $\sim 0.48 \text{ Na}$ , with a long voltage plateau at 3 V, operating between 3.6–2.0 V (as shown in Table 2). Therefore, maintaining the cycling performance of the fully charge–discharge process (one Na) remains challenging due to the irreversible structural evolution when  $x < 0.5$ . The latest study showcased that the inclusion of  $\text{Sb}^{5+}$  into the  $\text{NaCrO}_2$  lattice serves as an effective means to inhibit the migration of Cr, even under high charging voltages of up to 4.1 V (*vs.*  $\text{Na}^+/\text{Na}$ ). Remarkably, at a low current rate of C/20, the O3-type  $\text{Na}_{0.72}\text{Cr}_{0.86}\text{Sb}_{0.14}\text{O}_2$  cathode material demonstrated a notable specific capacity of approximately  $175 \text{ mA h g}^{-1}$ . This corresponds to 72% of  $\text{Na}^+$  undergoing deintercalation in  $\text{NaCrO}_2$  structure.<sup>163</sup>

### 4.3. $\text{Na}_x\text{MnO}_2$

$\text{Na}_x\text{MnO}_2$ , an early and extensively studied member of layered oxides,<sup>82</sup> exhibits metallic or semiconducting behavior

contingent on the M–M bond distance and the degree of d orbital overlap. These parameters critically govern the kinetics of the material.  $\text{Na}_x\text{MnO}_2$  can be classified into two structural categories: 3D structures (tunnel structures) denoted by  $x = 0.4$  and  $0.44$ , which have been extensively explored, notably in the context of aqueous electrolytes,<sup>164–166</sup> and 2D structures represented by  $x = 1.0$  and  $0.7$ . The latter encompasses three distinct phases: P2- $\text{Na}_{0.7}\text{MnO}_{2+y}$ ,<sup>167</sup>  $\alpha$ - $\text{NaMnO}_2$ ,<sup>86</sup> and  $\beta$ - $\text{NaMnO}_2$ .<sup>87</sup> The synthesis of P2- $\text{Na}_{0.6}\text{MnO}_2$  employed a sol-gel method incorporating  $\text{Mn}(\text{acetylacetonate})_3$ ,  $\text{Na}_2\text{CO}_3$ , and propionic acid to form the resin framework.<sup>167</sup> The correspondence between the discharge and charge profiles during the initial cycle underscores the material's ability to consistently furnish a specific capacity of *ca.*  $140 \text{ mA h g}^{-1}$  at a current density of  $0.1 \text{ mA cm}^{-2}$  within the voltage window of  $3.8$ – $2.0 \text{ V}$ . Recent reexamination of the electrochemical behavior of monoclinic  $\alpha$ - $\text{NaMnO}_2$  has yielded insights.<sup>86</sup> It demonstrated an initial discharge capacity of  $185 \text{ mA h g}^{-1}$  at a rate of  $0.1\text{C}$ , stabilizing at  $132 \text{ mA h g}^{-1}$  after 20 cycles. Noteworthy is the deintercalation/intercalation of approximately  $0.85/0.8 \text{ Na}$  from/into  $\text{NaMnO}_2$  during potentiostatical intermittent charge/discharge processes, yielding a significantly elevated capacity compared to prior investigations of  $\alpha$ - $\text{NaMnO}_2$ . While precise determinants underpinning this unexpected augmentation ( $185 \text{ mA h g}^{-1}$ ) remain elusive, the electrolyte composition ( $\text{NaPF}_6$  in EC-DMC) has been posited as a potential contributing factor. Furthermore, the scrutiny delved into  $\beta$ - $\text{NaMnO}_2$ , characterized by a distinct structure compared to extensively studied  $\text{NaMnO}_2$  polymorphs and compounds.<sup>87</sup> It showcased a substantial capacity of

approximately  $190 \text{ mA h g}^{-1}$  at a rate of  $\text{C}/20$  (as tabulated in Table 2), concomitant with commendable rate capability of  $142 \text{ mA h g}^{-1}$  at a current rate of  $2\text{C}$  and robust capacity retention of  $100 \text{ mA h g}^{-1}$  after 100 charge–discharge cycles.

Nevertheless, the structural instability exhibited by  $\text{Na}_x\text{MnO}_2$  due to the pronounced volume fluctuations during de/intercalation process remains a pivotal challenge. Furthermore, the distortion in  $\text{Na}_x\text{MnO}_2$  structures arising from the presence of high spin Jahn–Teller active  $\text{Mn}^{3+}$  ions engenders electronic localization and depresses the diffusion coefficient, thus posing intricate electronic and kinetic hurdles.<sup>168–170</sup> To address this issue, strategic intervention have been pursued, such as controlled partial substitutions involving Li, Ni and Co *in lieu* of Na in  $\text{Na}_x\text{MnO}_2$ . These substitutions hold the promise of inducing an orthorhombic or ideal P2 structure, thereby enhancing the structural resilience and stability of the material.<sup>171</sup> An alternative avenue involves the judicious incorporation of electrochemically inert elements *in lieu* of transition metals. An illustrative example is the introduction of  $\text{Al}^{3+}$  doping, which effectively increases the spacing between  $\text{Na}^+$  layers and mitigates Jahn–Teller distortions within  $\text{Na}_{0.67}\text{Al}_x\text{Mn}_{1-x}\text{O}_2$ , as shown in Fig. 3a. Notably, even at a modest  $\text{Al}^{3+}$  content of 10%, significant improvements were observed. This included the smoothing of charge–discharge profiles and the preservation of a high specific capacity (Fig. 3b and c).<sup>172</sup>

Incorporating Li into the transition metal (TM) layer of P2- $\text{Na}_{0.67}\text{Li}_{0.1}\text{Fe}_{0.37}\text{Mn}_{0.53}\text{O}_2$  (NLFMO) introduces additional oxygen redox activity, particularly at elevated charging voltages.<sup>173</sup> Fig. 4a illustrates the presence of the OP4 phase, acting as a boundary

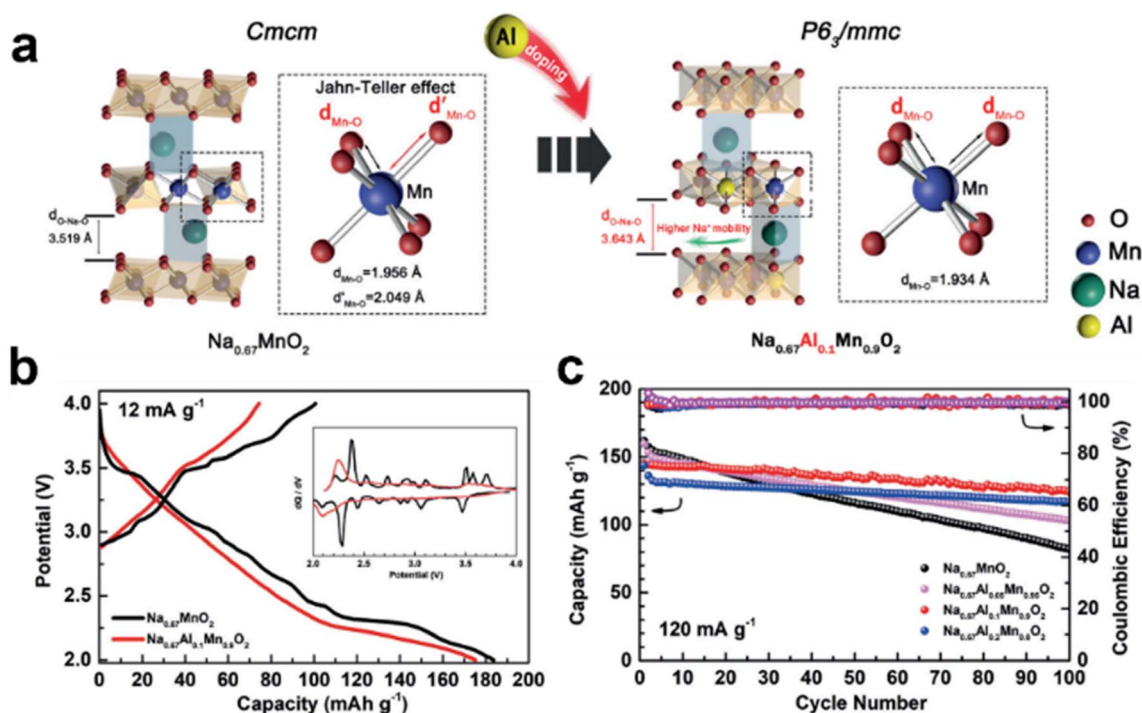
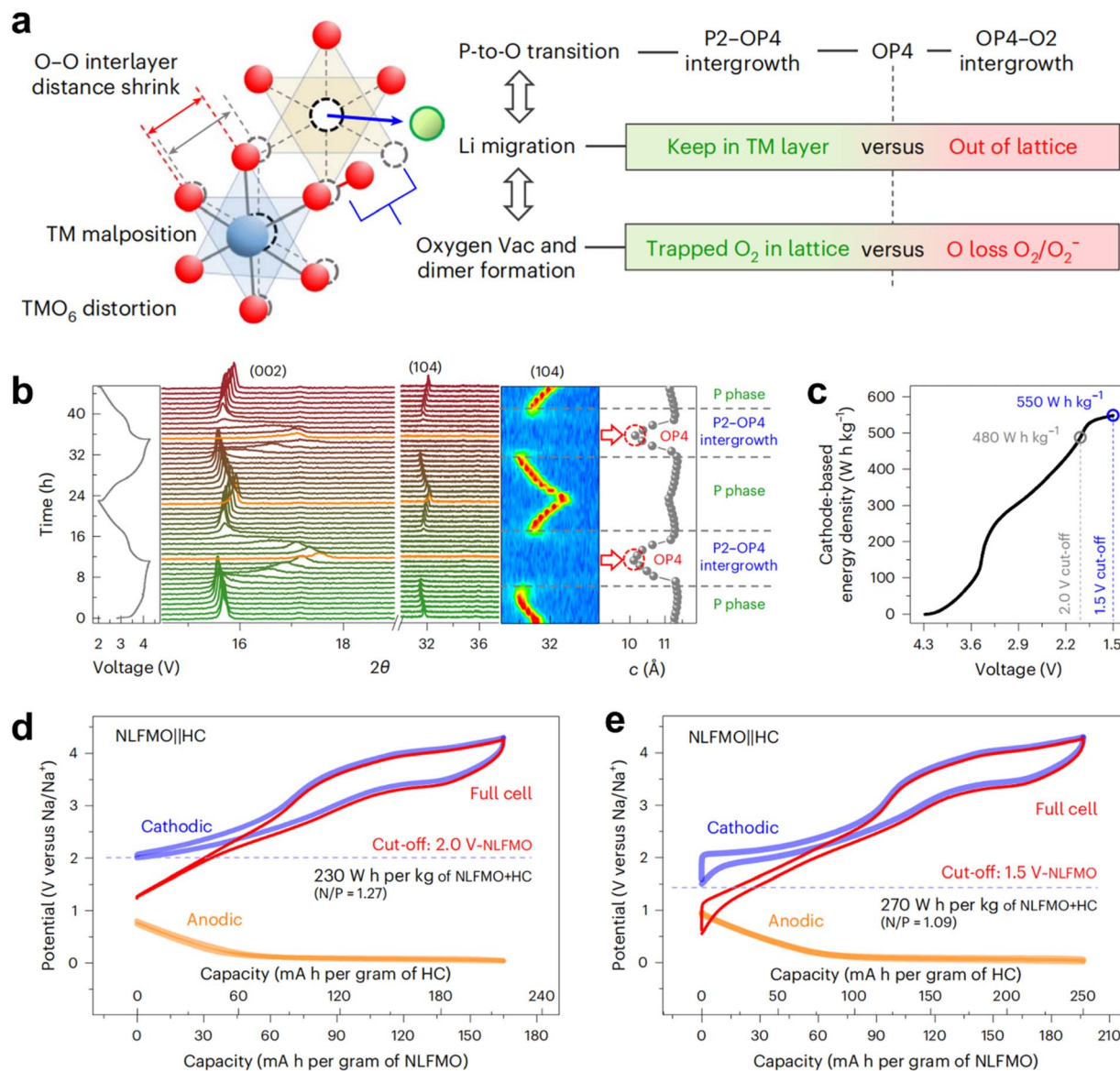


Fig. 3 Structural characterizations and electrochemical performances of  $\text{Al}^{3+}$  doped  $\text{Na}_{0.67}\text{MnO}_2$ . (a) Structural illustration of  $\text{Al}^{3+}$  doped  $\text{Na}_{0.67}\text{MnO}_2$ . (b) Charge/discharge profiles of  $\text{Na}_{0.67}\text{MnO}_2$  and P2- $\text{Na}_{0.67}\text{Al}_{0.1}\text{Mn}_{0.9}\text{O}_2$  at  $12 \text{ mA g}^{-1}$ . (c) Cycling performance of  $\text{Al}^{3+}$  doped  $\text{Na}_{0.67}\text{MnO}_2$  at  $\text{mA g}^{-1}$ . Reproduced from ref. 172 with permission from Wiley-VCH GmbH, copyright 2019.



**Fig. 4** (a) The diagram illustrates the  $\text{LiO}_6/\text{TMO}_6$  distortion in the charged  $\text{P2-Na}_{0.67}\text{Li}_{0.1}\text{Fe}_{0.37}\text{Mn}_{0.53}\text{O}_2$  (NLFMO) structure, as observed along the (001) direction, with red, blue and green balls representing O, TM and Li atoms, respectively. (b) *In situ* XRD patterns for the NLFMO cathode were obtained during the initial two charge–discharge cycles within the voltage range of 2.0–4.3 V. (c) The galvanostatic charge/discharge profiles of the NLFMO cathode indicate that increasing the lower cut-off voltage from 2.0 V to 1.5 V results in improved specific energy density. (d and e) The electrochemical profiles of the NLFMO cathode and hard carbon anode measured in a three-electrode cell within voltage windows of 2.0–4.3 V (c) and 1.5–4.3 V (d). Reproduced from ref. 173 with permission from Springer Nature, copyright 2024.

phase between the P2–OP4 and OP4–O2 intergrowth structures. Understanding the nuanced influence of the O/P intergrowth structure and precisely defining the OP4 boundary phase holds significant potential for enhancing both the reversible capacity and structural stability of P2-type cathodes. Further insights into reversible phase transitions were garnered from XRD patterns (Fig. 4b), confirming the presence of the OP4 phase at a charge cut-off SoC of 4.3 V. Despite the Jahn–Teller effects associated with  $\text{Mn}^{3+}$ , successfully extending the discharge cut-off voltage from 2.0 V to 1.5 V led to a notable increase in the cathode's specific energy density. This enhancement is striking, with the specific energy density rising from  $480 \text{ W h kg}^{-1}$  to an impressive

$550 \text{ W h kg}^{-1}$  (Fig. 4c). Moreover, by seamlessly integrating a hard carbon (HC) anode, full NLFMO||HC batteries were assembled in a three-electrode configuration. Operating within a cathode voltage window of 4.3 to 2.0 V vs.  $\text{Na}/\text{Na}^+$  (Fig. 5d), the specific energy density based on the weight of active materials was  $230 \text{ W h kg}^{-1}$ . Expanding the cathode cycling range to 4.3–1.5 V and reducing the N/P ratio to 1.09 led to a further increase in specific energy density, reaching  $270 \text{ W h kg}^{-1}$  (Fig. 5e).

#### 4.4. $\text{NaNiO}_2$

The O3-phase configuration of  $\text{NaNiO}_2$  exhibits an optimally hexagonal crystalline structure at temperatures surpassing

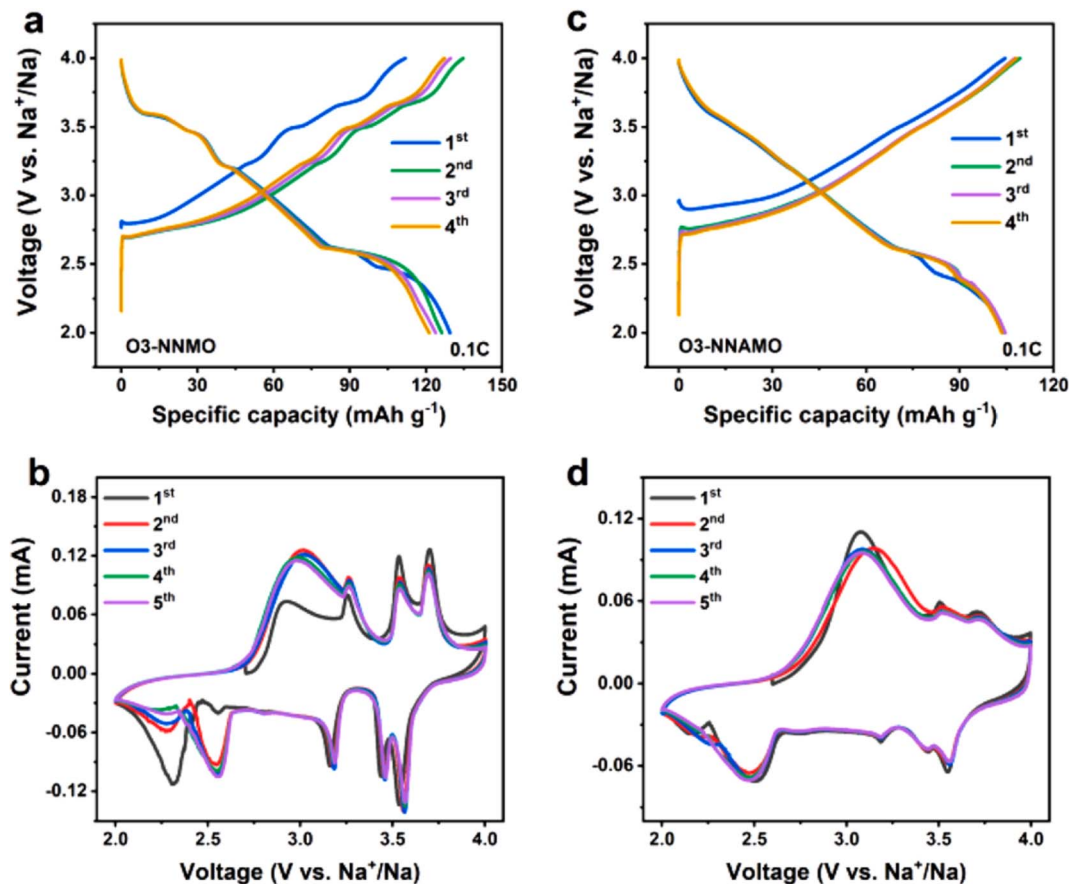


Fig. 5 (a) Galvanostatic charge–discharge curves at a rate of 0.1C and (b) corresponding CV curves at  $0.1 \text{ mV s}^{-1}$  of O3-phase  $\text{NaNi}_{0.5}\text{Mn}_{0.5}\text{O}_2$ ; (c) galvanostatic charge–discharge curves at a rate of 0.1C and (d) corresponding CV curves at  $0.1 \text{ mV s}^{-1}$  of  $\text{Al}^{3+}$  doped  $\text{NaNi}_{0.5}\text{Mn}_{0.5}\text{O}_2$ . Reproduced from ref. 174 with permission from Elsevier, copyright 2023.

220 °C, transitioning into a distorted monoclinic arrangement below this thermal threshold. The synthesis of O3-type  $\text{NaNiO}_2$  was initially accomplished by Braconnier *et al.*<sup>117</sup> in 1982, elucidating a modest de-intercalation of 0.2 Na per formula unit. In recent times, a renewed investigation into the electrochemical attributes of O3-type  $\text{NaNiO}_2$  has yielded noteworthy insights. The inaugural cycle revealed a high capacity (charge capacity:  $147 \text{ mA h g}^{-1}$ , discharge capacity:  $123 \text{ mA h g}^{-1}$ ) between 3.75–1.25 V at 0.1C – a discernible advancement compared to previous reports.<sup>88</sup>  $\text{NaNiO}_2$  showcased a de-intercalation of 0.85 Na juxtaposed with an intercalation of 0.65 Na (equating to the charge/discharge capacity 199 and  $147 \text{ mA h g}^{-1}$ , respectively) during cycling spanning 4.5 and 2.0 V at 0.1C. In consonance with initial observations, multiple voltage plateaus were manifest, maintaining fidelity to antecedent findings. However, it is noteworthy that rapid capacity degradation and a low coulombic efficiency of 86.3% at the 20th cycle were apparent. This conspicuous decline in capacity can be attributed to the inability to achieve a fully sodiated phase (characterized by a  $\text{NaNiO}_2$  composition) during the initial discharge process. A more comprehensive explication of this phenomenon, coupled with an in-depth exploration of the multifaceted phase transitions that transpire during cycling,

will be expounded upon in ensuing sections of this comprehensive review.

Thorough structural and electrochemical investigations into the incorporation of Li, Ti, Al, and Mn into  $\text{Na}_x\text{NiO}_2$  have illuminated a dual enhancement strategy, characterized by augmented structural stability and distinct (de)intercalation mechanisms within the material.<sup>174–177</sup> The typical charge/discharge curves of  $\text{NaNi}_{0.5}\text{Mn}_{0.5}\text{O}_2$ , as shown in Fig. 5a, demonstrate four distinct plateaus. The characteristics of the cyclic voltammetry (CV) curves, depicted in Fig. 5b, are consistent with the plateaus of the charge/discharge curves, indicating a complex phase transformation process of  $\text{O3}_{\text{hex}} - \text{O3}_{\text{mon}} - \text{P3}_{\text{hex}} - \text{P}'3_{\text{mon}} - \text{P}'3_{\text{hex}} - \text{O3}_{\text{hex}}$  during the charge/discharge process.<sup>174</sup> Further doping with  $\text{Al}^{3+}$  leads to smoother charge/discharge curves for Al-doped  $\text{NaNi}_{0.5}\text{Mn}_{0.5}\text{O}_2$  (Fig. 5c), which now exhibit only three plateaus. Correspondingly, the CV curves (Fig. 5d) also reflect these changes. Following  $\text{Al}^{3+}$  doping, the capacity retention rate of O3- $\text{NaNi}_{0.5}\text{Mn}_{0.5}\text{O}_2$  improves from 40.9% to 86.2% after 200 cycles at 0.5C.<sup>174</sup> The integration of titanium-doped structure, on the other hand, yields a distinct advantage of enhanced cycling stability, albeit accompanied by a marginal reduction in the initial reversible capacity.<sup>175</sup> A representative exemplar,  $\text{Na}_{2/3}\text{Ni}_{1/3}\text{Mn}_{1/2}\text{Ti}_{1/6}\text{O}_2$ , demonstrates a commendable reversible capacity of  $127 \text{ mA h g}^{-1}$ , accompanied

by an average discharge voltage of *ca.* 3.7 V, as observed in the initial cycle. Noteworthy is the discernible modification in voltage profiles for  $\text{Na}_{2/3}\text{Ni}_{1/3}\text{Mn}_{2/3}\text{O}_2$  upon titanium substitution. This shift serves as an indicative signal of the amelioration of Na/vacancy ordering, electronic/magnetic ordering, and/or phase transitions throughout the sodium intercalation process.<sup>97</sup>

The strategic introduction of a minor quantity of lithium substitution within the transition metal oxide layer emerges as a pivotal advancement, particularly in addressing the multifaceted intricacies inherent to multiple plateau behavior and the ensuing complex phase transitions.<sup>178</sup> Notably, the incorporation of a minute fraction of lithium into  $\text{Na}_{0.85}\text{Li}_{0.17}\text{Ni}_{0.21}\text{Mn}_{0.64}\text{O}_2$  yielded marked enhancements in charge–discharge performance, underscored by an average voltage of 3.4 V. The ensuing voltage profile portrayed a seamlessly evolving discharge/charge curve, indicative of singular-phase intercalation. In this context, Li within the transition metal site is poised to orchestrate a pivotal role in the electrochemical reaction mechanism. Remarkably, an exceptional rate capability was demonstrated, as evidenced by a reversible capacity of  $65 \text{ mA h g}^{-1}$  at the current density of  $1600 \text{ mA g}^{-1}$  (25C). Furthermore, materials exhibiting an average capacity within  $95\text{--}100 \text{ mA h g}^{-1}$  range experienced only a marginal 2% diminution of their initial capacity subsequent to 50 cycles at a current rate of  $15 \text{ mA g}^{-1}$ . This gradual attenuation in capacity can be attributed to a confluence of factors, including the pronounced first cycle irreversible capacity loss and subsequent coulombic inefficiency stemming from side-reactions with Na metal, in conjunction with the associated challenge of Na plating during the charge process. The indispensable role of lithium substitution in the context of  $\text{Na}_x[\text{Li}_y\text{Ni}_z\text{Mn}_{1-y-z}]\text{O}_2$  ( $0 < x, y, z < 1$ ) was further underscored through insights garnered from neutron diffraction, nuclear magnetic resonance (NMR) spectroscopy and *in situ* synchrotron X-ray diffraction, as delineated in forthcoming sections of this comprehensive review.<sup>176</sup>

In the pursuit of elevating specific capacity, meticulous investigation has centered on the Li-rich layered oxide, serving as a high-energy density cathode for LIBs.<sup>179,180</sup> A comprehensive examination has been conducted on a corresponding SIBs cathode, involving the activation of oxygen activity. An electrochemical Li/Na exchange strategy of the lithium analogous has revealed an approximate extraction of 1.08 Li ions and intercalation of 0.76 Na (equivalent to  $239 \text{ mA h g}^{-1}$ ) within the host structure. This phenomenon transpires across a voltage range of 4.5–1.7 V at a current density of  $5 \text{ mA g}^{-1}$ .<sup>181</sup> Kataoka *et al.*<sup>182</sup> prepared the Li-rich  $\text{Na}_{0.95}\text{Li}_{0.15}(\text{Mn}_{0.55}\text{Co}_{0.10}\text{Ni}_{0.15})\text{O}_2$  cathode using the similar approach. This material delivered a high capacity of  $238 \text{ mA h g}^{-1}$  within 1.0–4.2 V cycling and coulombic efficiency of 71% (corresponding to 85% of the second discharge capacity) after 40 cycles. The  $\text{Na}_{0.95}\text{Li}_{0.15}(\text{Mn}_{0.55}\text{Co}_{0.10}\text{Ni}_{0.15})\text{O}_2$  material retained its O3-type layered structure, exhibiting a substantial volume change of 20% during charging, accompanied by the formation of a second phase that shares the similar structure as  $\text{Na}_{0.95}\text{Li}_{0.15}(\text{Mn}_{0.55}\text{Co}_{0.10}\text{Ni}_{0.15})\text{O}_2$  at elevated voltages.

#### 4.5. Olivine $\text{NaMPO}_4$

Olivine  $\text{NaMPO}_4$  is not a thermodynamically stable structure, unlike  $\text{LiMPO}_4$  ( $M = \text{Fe, Mn, Co, etc.}$ ). However, the stable phase maricite  $\text{NaMPO}_4$ , in which the sites for  $\text{Na}^+$  and  $\text{Fe}^{2+}$  are opposite to those in olivine  $\text{LiMPO}_4$ , demonstrates limited electrochemical activity as mentioned before. The electrochemical performance of maricite  $\text{NaFePO}_4$  has been significantly improved by encapsulating them within a thin carbon layer (m-NFP@C).<sup>100</sup> The optimized m-NFP@C cathode maintained a reversible capacity of  $101.4 \text{ mA h g}^{-1}$  after 100 cycles, corresponding to a high capacity retention of 90.5%. Due to the ultrafine nanostructure of the m-NFP@C particles and their uniform carbon coating, the sodium-ion full cell demonstrates remarkable cycling stability and maintain 90.6% of its initial capacity through 250 cycles when coupled with a Bi@NC-MF anode. Both the ultrafine nanostructure and uniform carbon coating effectively facilitate  $\text{Na}^+$  diffusion and enhance electronic conductivity, thereby resulting in the achievement of excellent electrochemical performance. Additionally, olivine  $\text{NaFePO}_4$  has been successfully obtained through electrochemical Na insertion into heterosite  $\text{FePO}_4$ , a process achievable through chemical or electrochemical delithiation of olivine  $\text{LiFePO}_4$ .<sup>140,178</sup> In contrast to  $\text{LiFePO}_4$ , olivine  $\text{NaFePO}_4$  undergoes an intermediate phase transition to  $\text{Na}_{0.7}\text{FePO}_4$  at 2.95 V during the charging process, as illustrated in Fig. 6a and b.<sup>183</sup> Notably, the voltage profiles during charging and discharging exhibit a consistent voltage progression, indicative of a continuous single-phase redox reaction.<sup>186,187</sup>

#### 4.6. NASICON-type compounds

In the years 1987–1988, Delmas *et al.* unveiled the electrochemical activity of NASICON-type compounds, such as  $\text{NaTi}_2(\text{PO}_4)_3$ , in a reversible manner.<sup>188,189</sup> Subsequently, Yamaki and co-workers firstly reported on electrochemical activity of  $\text{Na}_3\text{V}_2(\text{PO}_4)_3$ , which can deliver discharge capacity of  $140 \text{ mA h g}^{-1}$  between 1.2–3.5 V. This capacity was ascribed to the participation of the  $\text{V}^{3+}/\text{V}^{4+}$  and  $\text{V}^{2+}/\text{V}^{3+}$  redox couples, with the  $\text{V}^{3+}/\text{V}^{4+}$  conversion contributing  $90 \text{ mA h g}^{-1}$  to this total capacity.<sup>190</sup> Specifically, the charge–discharge profiles manifested two distinct redox voltage plateaus at 3.4 V ( $\text{V}^{3+}/\text{V}^{4+}$ ) and 1.6 V ( $\text{V}^{2+}/\text{V}^{3+}$ ). However, only the higher voltage plateaus can deliver a reversible capacity while the lower redox voltage plateaus is hard to offer capacity in the practical battery systems. The typical electrochemical profiles of the NASICON  $\text{Na}_3\text{V}_2(\text{PO}_4)_3$  cathode are presented in Table 2.<sup>103</sup> Despite the constraints posed by the inactive M1 lattice sites during the insertion/extraction process, the reversible capacity based on the two-electron reaction mechanism remains unsatisfactory. To tackle this challenge, a facile electrostatic spray deposition method was developed for fabricating self-supporting 3D porous  $\text{Na}_3\text{V}_2(\text{PO}_4)_3$ (NVP) materials with adjustable crystallinity on carbon foam substrates. By precisely controlling the crystallinity, efficient activation of the  $\text{V}^{5+}/\text{V}^{4+}$  redox couple has been achieved, enabling three-electron reactions in NVP for sodium storage. Remarkably, a disorder structured NVP displays a discharge capacity of  $179.6 \text{ mA h g}^{-1}$ , attributing to the two-

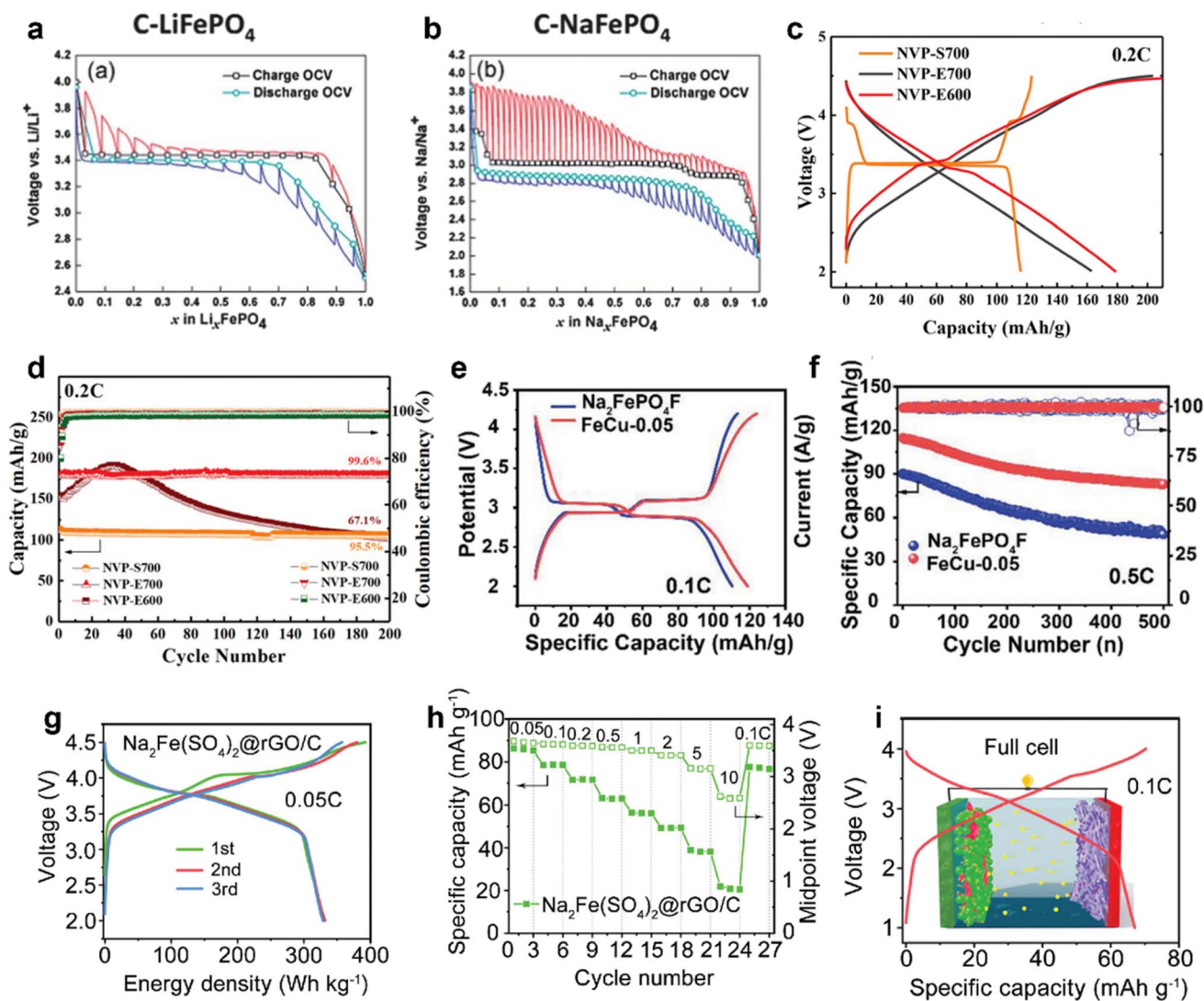


Fig. 6 (a) Equilibrium-voltage and transient voltage profiles vs. Li composition in C- $\text{Li}_x\text{FePO}_4$  obtained from GITT. (b) The comparison measurement for C- $\text{Na}_x\text{FePO}_4$ . Reproduced from ref. 183 with permission from the Royal Society of Chemistry, copyright 2013. (c) The initial charge-discharge curves and (d) Cycle performance of the NVP-S700, NVP-E700, and NVP-E600 at 0.2C. Reproduced from ref. 184 with permission from Wiley-VCH GmbH, copyright 2023. (e) Charge-discharge curves at 0.1C and (f) cycling performance at 0.5C of  $\text{Na}_2\text{FePO}_4\text{F}$  and FeCu-0.05. Reproduced from ref. 185 with permission from Wiley-VCH GmbH, copyright 2023. Sodium storage capability of  $\text{Na}_2\text{Fe}(\text{SO}_4)_2@r\text{GO}/\text{C}$  (g) voltage-energy density profiles at 0.05C rate for initial three cycles. (h) Cycle performance and (i) charge-discharge curves of the HC/G// $\text{Na}_2\text{Fe}(\text{SO}_4)_2@r\text{GO}/\text{C}$  full cell. Reproduced from ref. 148 with permission from Elsevier, copyright 2020.

electron redox reactions involving  $\text{V}^{4+}/\text{V}^{3+}$  and  $\text{V}^{5+}/\text{V}^{4+}$  redox couples (Fig. 6c and d).<sup>184</sup> The strategic incorporation of highly electronegative fluorine atoms into the covalent polyanionic framework significantly enhances the voltage of active redox couples, as demonstrated by compounds such as  $\text{Na}_2\text{FePO}_4\text{F}$ ,<sup>185</sup>  $\text{Na}_3\text{V}_2(\text{PO}_4)_2\text{F}_3$ ,<sup>191,192</sup> and  $\text{Na}_{1.5}\text{VPO}_4.8\text{F}_{0.7}$ .<sup>193</sup>  $\text{Na}_2\text{FePO}_4\text{F}$  shows great potential for improved sodium storage performance due to its robust structural stability, advantageous two-dimensional  $\text{Na}^+$  transfer pathways, and elevated working voltage. However, the limited number of active sodium sites and poor intrinsic electronic conductivity result in compromised rate capability and reduced reversible capacity. The substitution of  $\text{Cu}^{2+}$  leads to an elongation of the Na-O/F bond, reducing the effect of coordinated O near Na. This decrease the overpotential of the

material facilitates the activation of Na ions. Consequently,  $\text{Na}_2\text{Fe}_{0.95}\text{Cu}_{0.05}\text{PO}_4\text{F}/\text{C}$  cathode demonstrates an impressive rate capacity at a high current density of 20C ( $74 \text{ mA h g}^{-1}$ ) and a relatively high capacity of  $119 \text{ mA h g}^{-1}$  at a low rate of 0.1C (Fig. 6e).<sup>185</sup>

$\text{Na}_3\text{V}_2(\text{PO}_4)_2\text{F}_3$  (NVPF) distinguishes itself with its remarkable sodium-ion conductivity and a noteworthy operating voltage of 3.95 V (vs.  $\text{Na}^+/\text{Na}$ ), coupled with a theoretical specific capacity of  $128 \text{ mA h g}^{-1}$ . However, the practical utilization of NVPF is hindered by its inferior electronic conductivity, attributed to the presence of  $[\text{PO}_4]$  tetrahedral units within its structural matrix. To overcome this difficulty, a strategic approach involving surface modification with an N-doped carbon layer has been employed. The modified product is

called c-NVPF@NC which has significantly enhanced the electrochemical behavior of NVPF, evidenced by a notable specific capacity of 121 mA h g<sup>-1</sup> at 0.2C, 73.6 mA h g<sup>-1</sup> at 10C, and maintaining 82% of its initial discharge capacity after 500 cycles at 5C and 78% after 1000 cycles at 10C.<sup>191</sup> Na<sub>1.5</sub>VPO<sub>4.8</sub>F<sub>0.7</sub> offers an energy density of approximately 600 W h kg<sup>-1</sup>, a feat accomplished through a combination of multielectron redox reactions (involving 1.2 e<sup>-</sup> per unit) and the elevated potential of 3.8 V inherent to customized vanadium redox couple of V<sup>3.8+</sup>/V<sup>5+</sup>. Operating at a 0.1C rate, the discharge capacity of around 134 mA h g<sup>-1</sup> surpasses the theoretical capacity (129.7 mA h g<sup>-1</sup>) predicated on a one-electron transfer process. This material further underscores its excellence in cycling performance, preserving 95% of the initial capacity even after 100 cycles. Moreover, its prowess extends to prolonged usage, retaining over 83% and 84% of the initial capacity after 500 extended cycles at room temperature and a higher temperature of 60 °C, respectively.<sup>193</sup>

#### 4.7. Sulfates

Barpanda and co-workers unveiled a remarkable discovery in the form of a previously unknown material bearing a unique composition and structure, termed Na<sub>2</sub>Fe<sub>2</sub>(SO<sub>4</sub>)<sub>3</sub>. This extraordinary material showcases an unprecedented Fe<sup>3+</sup>/Fe<sup>2+</sup> redox potential, soaring to 3.8 V (vs. Na, and thus equivalent to 4.1 V vs. Li).<sup>55</sup> Notably, this achievement surmounts the previously established record in the Li-ion system, exemplified by Li<sub>1-x</sub>FeSO<sub>4</sub>F (with a potential of 3.9 V vs. Li, corresponding to 3.6 V vs. Na).<sup>194</sup> It is noteworthy that, in contrast to fluorosulphate cathodes, this elevated redox voltage was achieved without resorting to the inclusion of electronegative F<sup>-</sup> units, often utilized to bolster the voltage of active redox couples. For Na<sub>2</sub>-Fe<sub>2</sub>(SO<sub>4</sub>)<sub>3</sub>, the inaugural discharge capacity, a commendable 102 mA h g<sup>-1</sup> at a rate of C/20, corresponds to 85% of the theoretical one-electron capacity (ca. 120 mA h g<sup>-1</sup>), predicated on the Fe<sup>3+</sup>/Fe<sup>2+</sup> redox couple. This capacity retention has been demonstrated across 30 cycles, encompassing diverse discharge rates spanning from C/20 to 20C. The electrochemical process of desodiation–sodiation unfolds seamlessly, evident from the smooth and gradual charge–discharge profiles confined within a narrow voltage range of 3.3–4.3 V. This phenomenon attests to a unified, homogenous reaction mechanism. In a comparative analysis, the electrochemical activity of Na<sub>2</sub>Fe(SO<sub>4</sub>)<sub>2</sub>·4H<sub>2</sub>O was explored in both Na and Li cells.<sup>195</sup> However, the modest reversible capacities exhibited by the Na<sub>2</sub>Fe(SO<sub>4</sub>)<sub>2</sub>·nH<sub>2</sub>O compounds (n = 0 and 4), falling below 100 mA h g<sup>-1</sup>, limits their practical utility as electrode materials. Hierarchical Na<sub>2</sub>-Fe(SO<sub>4</sub>)<sub>2</sub>@rGO/C with 4.12 wt% carbon content, which was synthesized by Yao *et al.*, exhibits a brief voltage platform at around 3.75 V and achieves high energy density of ~330 W h kg<sup>-1</sup> in the initial three cycles at 0.05C (Fig. 6g). Furthermore, the rate performances of Na<sub>2</sub>Fe(SO<sub>4</sub>)<sub>2</sub>@rGO/C is exceptional, which can be fully verified by its ability to deliver reversible specific capacities of 40 mA h g<sup>-1</sup> and 22 mA h g<sup>-1</sup> even at higher current rates of 5C and 10C, respectively, as shown in Fig. 6h. Then a full cell, designated as HC/G//

Na<sub>2</sub>Fe(SO<sub>4</sub>)<sub>2</sub>@rGO/C, was assembled by the hard carbon/rGO composite as the anode and paired with the Na<sub>2</sub>Fe(SO<sub>4</sub>)<sub>2</sub>@rGO/C cathode. And it exhibits a capacity of 67 mA h g<sup>-1</sup> and an energy density of 196.67 W h kg<sup>-1</sup> at 0.1C (calculated based on the mass of the cathode material), as illustrated in Fig. 6i.<sup>148</sup>

#### 4.8. Prussian blue

The electrochemical activity and electrochromic behavior of Prussian blue (PB) were first unveiled by Neff in 1978.<sup>196</sup> The presence of water and vacancies plays a pivotal role in influencing the electrochemical performance of PB as cathode materials for SIBs. In the case of PB, the presence of [Fe(CN)<sub>6</sub>] vacancies can substantially reduce electronic conductivity, leading to a disordered lattice during cycling and potentially even causing framework collapse. In response to this challenge, researchers proposed high-quality PB crystals with a low crystal water content and a minimal number of [Fe(CN)<sub>6</sub>] vacancies.<sup>197</sup> This achievement was accomplished through the use of Na<sub>4</sub>-Fe(CN)<sub>6</sub> as the sole iron-source precursor, employing a straightforward synthetic method. The precipitation process from an acidic medium was meticulously controlled to yield materials of varying quality. Specifically, the material synthesized through a slower growth process resulted in high-quality (HQ)-NaFe nanocubes, characterized by a more crystalline structure. As a consequence, HQ-NaFe demonstrated an impressive specific capacity of 170 mA h g<sup>-1</sup>, achieved through a two-electron reaction mechanism. Furthermore, it exhibited remarkable cycling stability, sustaining its capacity without discernible degradation over 150 cycles. An electrochemically deposited thin film of the PB analogue, Na<sub>1.32</sub>Mn[Fe(CN)<sub>6</sub>]<sub>0.83</sub>·3.5H<sub>2</sub>O, has emerged as a promising cathode for SIBs.<sup>198</sup> This film showcased a charge capacity of 128 mA h g<sup>-1</sup>, closely approaching the theoretical value of 109 mA h g<sup>-1</sup> expected for a two-electron reaction. Remarkably, even after 100 cycles, the capacity retention remained at an impressive 87% of its initial capacity.

Furthermore, a versatile sodium composition denoted as Na<sub>2-x</sub>Fe[Fe(CN)<sub>6</sub>] was synthesized through a facile procedure employing Na<sub>4</sub>[Fe(CN)<sub>6</sub>] as the precursor. A series of sodium-rich Na<sub>2-x</sub>FeFe(CN)<sub>6</sub> compounds were synthesized *via* the chemical precipitation method. Among these, Na<sub>1.73</sub>Fe[Fe(CN)<sub>6</sub>]·3.8H<sub>2</sub>O exhibited exceptional cycling stability, notable initial coulombic efficiency, and outstanding rate capability. Moreover, on a larger scale, a synthesized PB variant sustained an impressive lifespan of 1000 cycles within a pouch full cell.<sup>158</sup> While these compounds showcase exceptional electrochemical properties, are non-toxic, and cost-effective, potential environmental concerns associated with their production processes or precursor materials warrant further scrutiny. Moreover, the challenge of precisely controlling water content during synthesis remains a pivotal factor significantly influencing their energy storage performance.<sup>158</sup>

The role of water in Prussian white (PW) systems significantly impacts their electrochemical performance during sodium ion storage. Maddar *et al.* expanded their investigation beyond material-level dehydration to encompass water-processed composite electrodes. They discovered that the

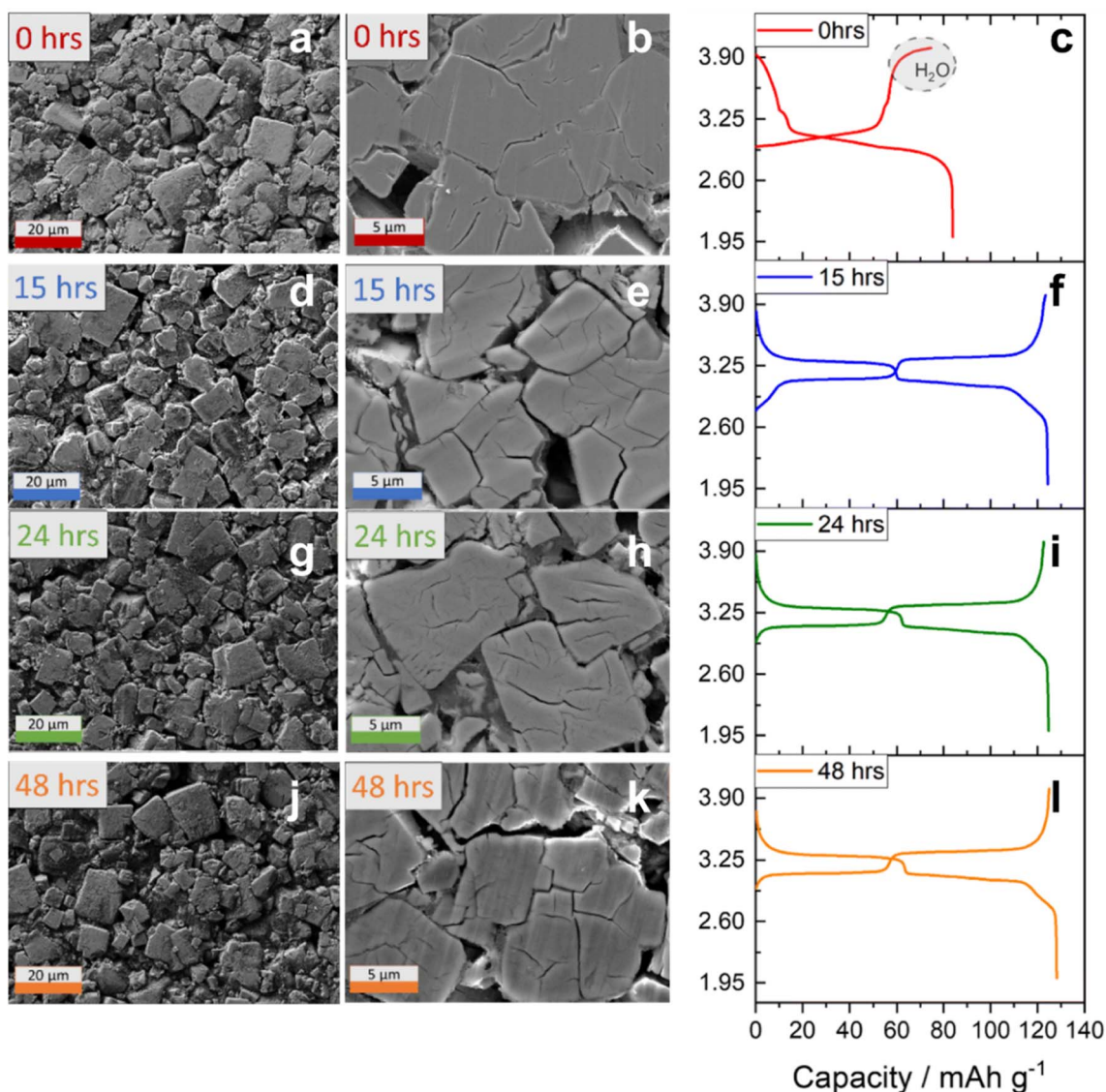


Fig. 7 SEM images of Prussian white (PW) electrodes dried for 0 (a and b), 15 (d and e), 24 (g and h) and 48 hours (j and k) at 170 °C; first charge/discharge curves of the PW electrodes dried for 0 (c), 15 (f), 24 (i) and 48 hours (l) at 0.1C. Reproduced from ref. 199 with permission from the Royal Society of Chemistry, copyright 2023.

dehydration process, influenced by variables like temperature and heating rate, becomes more intricate for composite electrodes. This complexity is evidenced by the delayed transition from hydrated monoclinic to dehydrated rhombohedral phases under low vacuum conditions. Optimal dehydration is achieved at temperatures between 170 °C under an efficient vacuum, yielding a material dominated by the rhombohedral phase with a capacity of 140 mA h g<sup>-1</sup> (Fig. 7).<sup>199</sup>

Berlin green can be synthesized from Prussian white by employing a chemical sodium extraction process. Similar to Prussian blue, Berlin green is highly sensitive to water content. Ojwang *et al.* systematically investigated Berlin green (Na<sub>0.30(5)</sub>Fe[Fe(CN)<sub>6</sub>]<sub>0.94(2)</sub>·*n*H<sub>2</sub>O) with varying water content (10, 8, 6, and 2 wt%). Their results demonstrate that thermal dehydration significantly improves cycling stability. The fully dehydrated Berlin green exhibits a high specific capacity of

approximately 60 mA h g<sup>-1</sup> and achieves long-term cycling performance over 300 cycles with a coulombic efficiency exceeding 99.9%.<sup>200</sup>

## 5. Advanced characterizations for cathode materials

A thorough understanding of the intricate reaction mechanisms that transpire during charge–discharge processes is best facilitated by harnessing the power of *in situ/operando* and *ex situ* measurement techniques. In view of this, we have meticulously compiled a comprehensive overview of these techniques as they are applied to cathode materials within sodium-ion batteries. This compilation is poised to provide valuable insights into the underlying intricacies of these processes, thereby enabling

a more nuanced comprehension of battery performance and behavior.

### 5.1. X-ray diffraction

X-ray diffraction (XRD) is a methodology grounded in the phenomenon of X-ray scattering by atoms arranged in a periodic manner within a crystal lattice, yielding a distinctive diffraction pattern corresponding to the crystallographic arrangement. Within the realms of both *in situ* and *ex situ* approaches, XRD serves as an invaluable tool for tracking the dynamic structural changes experienced by the material during the desodiation–sodiation process. By leveraging the XRD technique, the evolving structural characteristics of the material can be meticulously monitored and deciphered throughout these electrochemical processes.<sup>201</sup>

In the realm of investigating the charge–discharge process of  $\text{P2-Na}_x\text{CoO}_2$ , a comprehensive exploration was carried out utilizing *in situ* synchrotron XRD measurements, as elucidated in Fig. 8a.<sup>77</sup> This insightful study, uncovered noteworthy findings. From the initial as-deintercalated state to the ultimate discharge state situated below 2.3 V vs.  $\text{Na}^+/\text{Na}$ , a distinct trend emerged in the displacement of the (008) diffraction peak, manifesting as a shift towards higher  $2\theta$  angles. This prevalent phenomenon, commonly encountered in the domain of  $\text{A}_x\text{MO}_2$  layered oxides,<sup>203,204</sup> offered a clear indication that the decrease in the  $c_{\text{hex}}$  parameter could be attributed to an enhancement in the cohesiveness of the structural framework, facilitated by sodium intercalation. Simultaneously, a marginal elevation in the  $a_{\text{hex}}$  parameter underscored the augmentation of the M–M distance within the slabs, a consequences of  $\text{M}^{4+}$  reduction. Throughout the discharge process, a fascinating occurrence emerged – the (008) diffraction peak intermittently split into two, signifying the presence of a two-phase domain. This intriguing behavior coincided with potential plateaus discernible in the discharge curve. Notably, each potential drop was intricately linked to a solitary (008) diffraction peak. The subtle shift observed in its  $2\theta$  position provided a glimpse into the adoption of a slight solid-solution behavior within the single-phase domain. In contrast, a steadfast and unchanging  $2\theta$  position during the potential drop offered irrefutable evidence of the existence of a singular phase characterized by a precisely defined composition.

The investigative potential of *in situ* and *ex situ* XRD techniques was harnessed to unravel the intricate electrochemical reaction mechanism underlying the  $\text{NaNiO}_2$  cathode material. This comprehensive study offered profound insights into the material's behavior.<sup>119</sup> Notably, a multitude of stacking configurations, encompassing various distorted O3 and distorted P3 transitions were observed during the initial charge/discharge process (Fig. 8b).<sup>97</sup> An intricate evolution unfolded during cycling, with the emergence of two distinct phases: a monoclinic O3 structure (referred to as  $\text{O}''3$ ) during the charge (and/or conclusion of discharge) process, and a P3 structure (termed  $\text{P}'''3$ ) at 3.38 V, manifesting solely during the charging process. Significantly, the composition of the newfound  $\text{O}''3$ -phase corresponded to  $\text{Na}_{0.83}\text{NiO}_2$ , standing as the closest to achieving

a fully sodiated phase during the discharge process. Furthermore, the novel  $\text{P}'''3$ -phase was approximately reflective of  $\text{Na}_{0.50}\text{NiO}_2$  in composition. These insightful discoveries not only shed light on the complex phase transitions but also enhance our understanding of the underlying electrochemical mechanisms governing the behavior of  $\text{NaNiO}_2$  as a cathode material.

The investigation into the Na-driven structural transformations and (de)intercalation mechanisms of  $\text{Na}_x\text{Ni}_{1/3}\text{Co}_{1/3}\text{Mn}_{1/3}\text{O}_2$  was conducted *via in situ* XRD during the first charge process.<sup>205</sup> This meticulous study, provided valuable insights into the evolving phase landscape during the sodium deintercalation. The *in situ* XRD profile disclosed an initial rhombohedral O3-type phase accompanied by a minor presence of O1-type monoclinic phase. As the sodium deintercalation progressed, a notable shift emerged, characterized by diminishing O1 phase intensity alongside a concomitant rise in P3 (rhombohedral) phase intensity. This shift was indicative of the emergence of a biphasic domain (O1 + P3) corresponding to a range of  $0.9 < x < 0.82$ . Upon reaching  $x = 0.67$ , a distinct monoclinic peak splitting at  $54^\circ$  was observed, signifying the transition to the P1 phase. This transition was followed by the appearance of a small biphasic region (P1 + P3) for  $0.67 < x < 0.6$ . Subsequently, for  $x$  values at and below 0.6, a solid solution of P3-type emerged. The XRD profiles, aligned with the voltage profile, exhibited a staircase-like pattern, each step being associated with the formation of distinct phases, including O3, O1, P3, and P1. The reinsertion of sodium in  $\text{Na}_x\text{Ni}_{1/3}\text{Co}_{1/3}\text{Mn}_{1/3}\text{O}_2$  led to sequential phase transitions encompassing both biphasic and monophasic domains. This composition-driven structural evolution in  $\text{Na}_x\text{Ni}_{1/3}\text{Co}_{1/3}\text{Mn}_{1/3}\text{O}_2$  followed a sequenced progression: O3  $\rightarrow$  O1  $\rightarrow$  P3  $\rightarrow$  P1 phases, with an observed increase in the  $c$  parameter, while the  $a$  parameter remained relatively stable. These findings illuminate the nuanced interplay between composition and structural dynamics, underscoring the intricate mechanisms at play within this cathode material.

An insightful analysis into the electrochemical degradation of Fe-based layered oxides in SIBs was demonstrated utilizing *in situ* XRD measurements.<sup>125</sup> The study provided valuable insights into the nuanced phase transitions underlying the observed battery behavior. The investigation highlighted an overarching trend in phase transition, characterized by a relatively smooth and continuous progression. Specifically, the appearance and disappearance of the monoclinic structure (referred to as  $\text{m-N}_{1-x}\text{FO}$ ) exhibited a remarkable symmetry, reverting seamlessly during both charge and discharge processes. This symmetrical evolution, integral to the material's behavior, played a pivotal role in comprehending its performance degradation. Notably, the  $\text{m-N}_{1-x}\text{FO}$  phase emerged towards the end of the charging step and gradually dissipated during discharge. However, a distinct asymmetry characterized the phase evolution of the  $\text{O}''3\text{-N}_{1-x}\text{FO}$  phases between the charge and discharge processes. It was only at the termination of the discharge phase that the  $\text{O}''3$  phase transformed into the O3 phase. This asymmetry persisted across subsequent charge and discharge cycles (Fig. 8c). Although the signal intensities in



the subsequent cycles were diminished due to the reduced Na<sup>+</sup> ions cycling, the asymmetric phase transition behavior of the O'3 phase remained conspicuous. By employing *in situ* XRD analysis, the intricate phase dynamics that underlie the performance degradation of Fe-based layered oxides in SIBs was successfully uncovered. This investigation contributes to a deeper understanding of the material's behavior and sets the stage for further advancements in sodium-ion battery technology.

The sodium extraction mechanism from Na<sub>3</sub>V<sub>2</sub>(PO<sub>4</sub>)<sub>2</sub>F<sub>3</sub> has long been characterized in the literature as a straightforward solid solution process. However, recent investigations have hinted at a more intricate phase diagram, prompting a deeper exploration into its complexity. In this context, comprehensive studies were conducted to elucidate this intriguing phase diagram, uncovering a series of intermediate crystallizations that deviate from the conventional narrative (Fig. 8d).<sup>202</sup> Significantly, the lower voltage region of the phase diagram exhibited behavior that deviated from the conventional solid solution progression. Instead, it revealed three distinct biphasic reactions, each comprising two intermediate phases: Na<sub>2.4</sub>V<sub>2</sub>(PO<sub>4</sub>)<sub>2</sub>F<sub>3</sub> and Na<sub>2.2</sub>V<sub>2</sub>(PO<sub>4</sub>)<sub>2</sub>F<sub>3</sub>. Particularly noteworthy was the stabilizing influence of Na<sub>2.4</sub>V<sub>2</sub>(PO<sub>4</sub>)<sub>2</sub>F<sub>3</sub>, which engendered an ordering extending over a longer range, evidenced by a *d*-spacing of approximately 18 Å, indicative of a superstructure arrangement. Subsequently, the phase Na<sub>2</sub>V<sub>2</sub>(PO<sub>4</sub>)<sub>2</sub>F<sub>3</sub> emerged at the conclusion of the first voltage plateau, hinting at a possible superstructure resulting from sodium and/or charge ordering. The higher voltage plateaus region introduced another layer of complexity, featuring a biphasic reaction leading to the disappearance of Na<sub>2</sub>V<sub>2</sub>(PO<sub>4</sub>)<sub>2</sub>F<sub>3</sub>. Subsequently, a wide solid solution range encompassing compositions denoted as Na<sub>*x*</sub>V<sub>2</sub>(PO<sub>4</sub>)<sub>2</sub>F<sub>3</sub> (1.8 ≤ *x* ≤ 1.3) emerged, characterized by sodium-disordered arrangements. Ultimately, the terminal NaV<sub>2</sub>(PO<sub>4</sub>)<sub>2</sub>F<sub>3</sub> end-member emerged through yet another biphasic reaction. Remarkably, this structure exhibited a distinctive *Cmc*2<sub>1</sub> space group, marked by a fully occupied sodium site and, intriguingly, two distinct vanadium environments within each bioctahedron, representing a V<sup>3+</sup>–V<sup>5+</sup> couple.<sup>206–208</sup> The comprehensive study underscored the significance of improved angular resolution and high-intensity diffraction data, pivotal factors enabling the direct observation of intricate reaction pathways within electrode materials. The insights gained through this investigation proved invaluable in comprehending the intricate (de)intercalation mechanisms underpinning SIBs.

## 5.2. X-ray absorption spectroscopy

X-ray absorption spectroscopy (XAS) serves as a powerful analytical tool for discerning the local geometric and electronic attributes of a material, thereby facilitating a more profound comprehension of the redox processes inherent to battery systems.<sup>209</sup> This technique dissects the absorption spectra into two primary regions, namely the X-ray near-edge spectroscopy (XANES) and the extended X-ray absorption fine structure (EXAFS). XANES imparts insights into the oxidation state of the

material, furnishing a nuanced understanding of its electronic configuration. This facet of XAS aids in unraveling the intricate interplay of electron transfer and charge redistribution during battery cycling. In contrast, EXAFS serves as an invaluable conduit for obtaining intricate molecular structure information. By scrutinizing the subtle deviations from perfect crystallinity, EXAFS facilitates the characterization of local coordination environments and bond distances, thereby enhancing our grasp of the intricacies governing redox reactions within battery materials. By capitalizing on the unique advantages offered by both XANES and EXAFS, X-ray absorption spectroscopy emerges as a pivotal tool for unraveling the multifaceted electrochemical transformations occurring within battery electrode materials.

The Mn K-edge XANES spectra of Zn-doped Na<sub>*x*</sub>MnO<sub>2</sub> (NZM) and pristine Na<sub>*x*</sub>MnO<sub>2</sub> (NM) electrodes exhibit distinct features, including pre-edge peaks (P1 and P2), a shoulder peak (A), and a main white-line peak (M) (Fig. 9a–c). These features reflect alterations in the electronic structure during redox reactions. Upon charging, the intensities of the pre-edge peaks (P1 and P2) increase in the NZM electrode, indicating heightened structural disorder due to reactive redox involving oxygen within the lattice. The subsequent restoration of pre-edge peak intensities upon sodium insertion suggests the high reversibility of Mn redox in NZM. Conversely, the interval between P1 and P2 decreases in the NM material, indicative of structural changes consistent with HEXRD (high-energy X-ray diffraction) findings. The peak labeled A corresponds to the hybridization of 4p–3d states. The reduced peak A intensity after initial charging indicates an increase in Mn 3d states, suggesting electron transfer from the 2p states of oxygen to the 3d states of Mn. The primary peak M shifts to higher energy upon initial charging, signifying Mn oxidation, and shifts to lower energy during discharge, reflecting a reduction in the valence state of Mn ions. Smaller energy shifts of peak M in NZM compared to NM indicate a higher Mn valence in NZM. *In situ* EXAFS spectra revealed that peaks at ≈1.3 and 2.5 Å corresponded to Mn–O bonds and Mn–Mn atom pairs, respectively. The Mn–O bond positions and intensities changed slightly in NZM, suggesting stable local MnO<sub>6</sub> octahedra. In contrast, the EXAFS peak intensities for NM varied significantly, indicating structural changes during cycling, consistent with HEXRD results (Fig. 9d–f). Overall, the X-ray absorption spectroscopy results provided insights into the electronic and structural changes in both NZM and NM electrodes during redox reactions, highlighting the differences in their behavior and stability during charge and discharge cycles. This in-depth study demonstrates the pivotal role of XAS in understanding the reaction mechanisms of battery materials that involve both chemical and physical structures.<sup>210</sup>

## 5.3. Nuclear magnetic resonance spectroscopy

Nuclear magnetic resonance (NMR) stands as a versatile technique that harnesses the magnetic properties inherent to specific atomic nuclei, thereby enabling the extraction of valuable insights into the physical and chemical attributes of atoms or molecules. This powerful method capitalizes on the nuclear

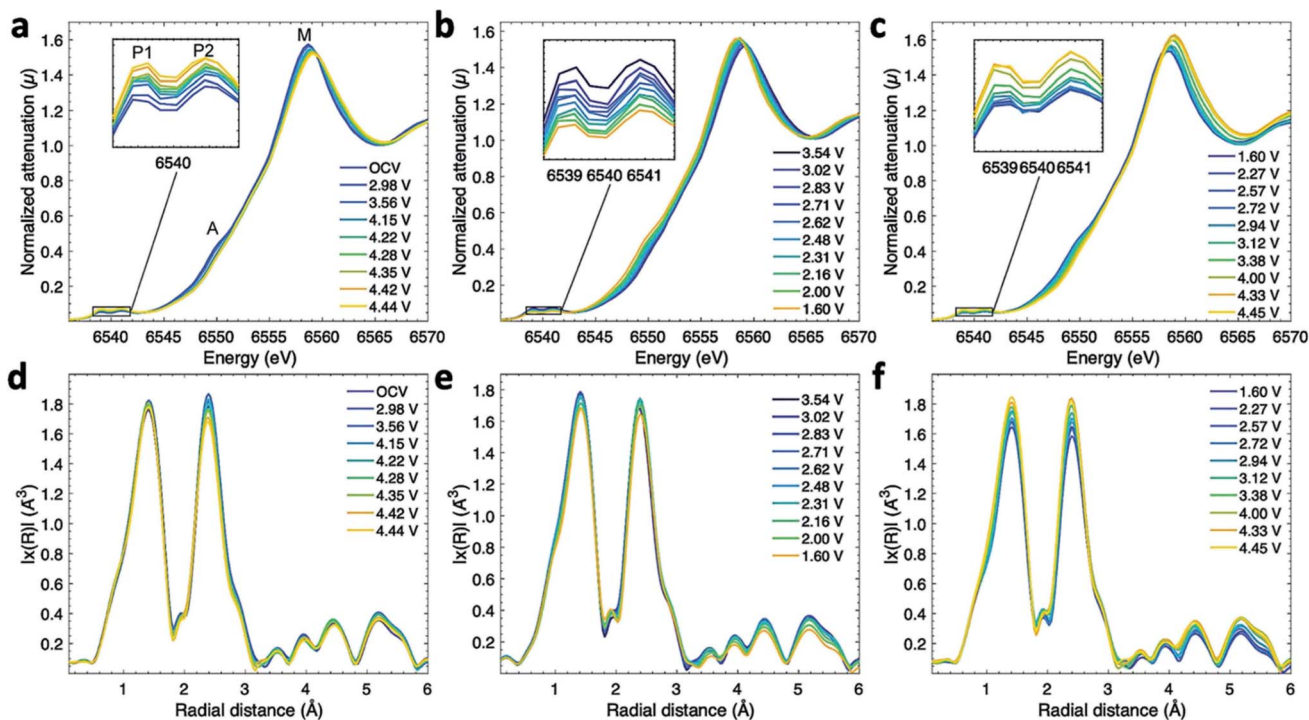


Fig. 9 (a–c) *In situ* Mn K-edge XANES spectra, and (d–f) the Fourier transformed EXAFS spectra of the NZM electrode during the initial charge process, initial discharge process, and second charge process, respectively. Reproduced from ref. 210 with permission from Wiley-VCH GmbH, copyright 2020.

magnetic resonance phenomenon to furnish comprehensive data concerning the structure, dynamics, reaction states, and chemical milieu of molecules. By probing the distinct local electronic environments of nuclei such as  $^7\text{Li}$  and  $^{23}\text{Na}$ , NMR holds the capability to adequately unravel pertinent details about the surrounding environment of lithium or sodium atoms. Consequently, NMR analysis provides an intricate window into the electrochemically induced structural changes that transpire within electrode materials throughout the cycling process.

The pivotal role of Li substitution in  $\text{P2-Na}_x[\text{Li}_y\text{Ni}_z\text{Mn}_{1-y-z}]\text{O}_2$  ( $0 < x, y, z < 1$ ) cathode materials has been deciphered through a combination of neutron diffraction, *in situ* XRD, and *ex situ* nuclear magnetic resonance (NMR) and XAS measurements.<sup>176</sup> The multi-faceted approach allowed for a comprehensive understanding of the intricate interplay of Na-ion dynamics and site occupation changes within the material. *Ex situ* NMR investigations were carried out on samples at various states of charge/discharge, facilitating the tracking of alterations in Li-ion site occupancy. Detailed 1D slices of the  $^7\text{Li}$  isotropic shifts provided a visual representation of the evolving  $^7\text{Li}$  local environments as a function of state of charge. Notably, the  $^7\text{Li}$  NMR spectra obtained during charging at 4.1 V and discharging at 2 V closely resembled the spectrum of the pristine sample. However, significant shifts in the relative occupation of Li local environments were observed within the voltage range of 4.1 to 4.4 V during charge. A particularly intriguing finding was the mobility of Li ions within the material. Some Li ions exhibited migration from the transition metal layer to the

sodium layer at higher voltages, yet this phenomenon demonstrated a remarkable degree of reversibility. These intriguing observations hold the potential to shape novel design principles for sodium cathode materials, grounded in an atomistic understanding of the underlying electrochemical process.

In the pursuit of comprehending the electrochemical reaction mechanisms, the NMR technique was extended to  $\beta\text{-Na}_x\text{-MnO}_2$  during the dynamic charge–discharge processes, unraveling essential insights into the underlying phenomenon.<sup>87</sup> The  $^{23}\text{Na}$  NMR spectra, acquired at varying sodium compositions, painted a revealing picture of evolving sodium environments within the material. Remarkably, the relative intensities of the two major peaks exhibited a continuous decline as sodium was progressively extracted from the system. What's noteworthy is the differential rate of decrease between the peak corresponding to the  $\beta$  environment and the peak associated with sodium at stacking faults. This contrast hinted at the selective extraction of sodium from the  $\beta\text{-NaMnO}_2$  phase, instigating the formation of more planar defects as sodium ions were removed. Consequently, this structural alteration led to a reduction in the concentration of  $\text{Na}^+$  ions in pure  $\beta$  environments, while concurrently increasing the  $\text{Na}^+$  presence in the stacking fault environment. Spectral integration unveiled a near 2 to 1 ratio between two major Na environments, signifying their coexistence within the material. Further exploration *via*  $^{23}\text{Na}$  NMR not only highlighted the occurrence of intermediate Na sites nestled between the ideal  $\alpha$  and  $\beta$  polymorphic forms but also elucidated their presence in the vicinity of planar defects bridging the two polymorphs. This complex interplay

had implications for the material's electrochemical properties. Specifically, the collapse of the long-range structure order at low Na content was anticipated to compromise the reversibility of the charge and discharge processes. These findings collectively contribute to a deeper comprehension of the intricacies governing the electrochemical behavior of SIB cathode materials.

#### 5.4. Mössbauer spectroscopy

Indeed, akin to NMR spectroscopy, Mössbauer spectroscopy serves as a powerful tool for investigating minute alterations in the energy levels of atomic nuclei in response to their surroundings. Within this technique, two distinct types of nuclear interactions come into play: the isomeric shift, also referred to as the chemical shift, and the quadrupole interaction. These interactions provide invaluable insights into the valence state and electronic configuration of the Mössbauer atom, ultimately shedding light on the intricate details of its atomic environment. By harnessing these spectroscopic nuances, researchers are empowered to unravel the complex interplay between atomic nuclei and their surrounding electronic structures, enriching our understanding of the underlying nature of materials and their behavior.

The role and stability of  $\text{Fe}^{4+}$  within the charged  $\text{Na}_x\text{FeO}_2$  electrodes were meticulously scrutinized using *ex situ* Mössbauer spectroscopy, a technique that offers insights into nuclear interactions.<sup>125</sup> In the pristine electrode spectrum, a symmetric absorption doublet was discernible, emblematic of the quadrupole splitting of  $\text{Fe}^{3+}$ . However, the charged material at a state of charge of 0.46 exhibited an asymmetric spectrum, resonating with the nominal composition of  $\text{Na}_{0.54}\text{FeO}_2$ . This asymmetry pointed to the presence of  $\text{Fe}^{4+}$  species. Intriguingly, the quantification of  $\text{Fe}^{4+}$  concentration (40.2%) through peak integration fell short of the anticipated value (46%) for nominal  $\text{Na}_{0.54}\text{FeO}_2$ . This discrepancy hinted at the involvement of parasitic reactions, such as solid–electrolyte interface (SEI) formation, that had an impact on the  $\text{Fe}^{4+}$  concentration. Notably, after a 2 days period of storing, the relative concentration of  $\text{Fe}^{4+}$  species declined to a mere 32%, a substantial reduction compared to that of  $\text{Na}_{0.5}\text{FeO}_2$ . This significant diminution in  $\text{Fe}^{4+}$  concentration subsequent to open-circuit storage in a charged state corroborates the chemical instability of  $\text{Fe}^{4+}$  species within  $\text{Na}_{1-x}\text{FeO}_2$ . These findings underscore the intricate chemical dynamics at play within the electrode materials and their implications for the overall electrochemical performance.

#### 5.5. Transmission electron microscopy

Transmission electron microscopy (TEM) is a powerful microscopy technique that involves transmitting a beam of electrons through a sample, enabling the construction of atomic-scale images. The *in situ* TEM technique holds the capability to detect atomic-scale structural changes occurring during battery operation. Additionally, electron diffraction and electron energy loss spectroscopy (EELS) can be employed to glean insights into the local composition and structure of materials. Notably, the pioneering work by Huang *et al.* in 2010,

focusing on a single  $\text{SnO}_2$  nanowire, marked the inception of *in situ* TEM studies.<sup>211</sup> Since then, numerous investigations have been conducted on nanostructured electrodes, primarily for lithium-ion batteries (LIBs) and anode materials in sodium-ion batteries (SIBs). These endeavors have provided invaluable insights into the dynamic behavior of materials at the nanoscale during electrochemical processes, paving the way for enhanced battery design and performance optimization.

TEM stands as a remarkable technique that enables the examination of the atomic-scale structural evolution of electrode materials *operando* conditions. Notably, *ex situ* TEM experiments have been conducted on  $\text{Na}_x\text{CrO}_2$  to unravel the intricate processes of intercalation and de-intercalation.<sup>212</sup> The electron diffraction patterns have unveiled a series of structural transformation steps encompassing O3  $\text{Na}_3\text{CrO}_2$ , P'3  $\text{Na}_{0.4}\text{CrO}_2$  and rock-salt  $\text{CrO}_2$  phases. A two-step progression characterizes this transformation: (i) the transformation of the P'3 structure of  $\text{Na}_{0.4}\text{CrO}_2$  into an O3 structure, which involves layer sliding and the extraction of  $\text{Na}^+$  ions, and (ii) the disproportionation of  $\text{Cr}^{4+}$ , resulting in the formation of  $\text{Cr}^{6+}$  species. The  $\text{Cr}^{6+}$  ions then proceed to move into the tetrahedral sites within the Na layer of the intermediate O3 structure. The formation of intermediate phase with compositions approximating  $\text{Na}_{\approx 2/3}\text{FePO}_4$  has been observed in  $\text{NaFePO}_4$ . *Ex situ* TEM studies have been instrumental in shedding light on the crystal structure of these intermediate phases. Notably, a supercell structure has been observed, formed through Na/vacancy and charge ordering mechanisms, enhancing our comprehension of these intricate electrochemical processes.<sup>60</sup>

#### 5.6. Transmission X-ray microscopy

Transmission X-ray microscopy (TXM) stands as a real-space imaging technique that enables direct, non-destructive investigation of material properties at the nanoscale. Its potential is magnified when coupled with X-ray absorption spectroscopy (including X-ray absorption near edge structure, XANES and extended X-ray absorption fine structure, EXAFS) or X-ray fluorescence techniques, facilitating the spatial acquisition of chemical information on battery particles. This approach sheds light on the distribution of chemical states within the material.<sup>213</sup> Notably, the excellent penetration capabilities of synchrotron-based X-ray sources empower *operando* TXM experiments during battery operation. These experiments yield fresh insights into the electrochemical reaction mechanism, thereby guiding improved battery materials and electrode designs.<sup>214</sup>

Leveraging advanced synchrotron-based real-space imaging techniques, we have delved into the realm of SIB battery materials to unravel the intricacies of electrochemical reaction mechanisms at the particle length scale. For instance, our investigations shed light on the inhomogeneous phase transformation mechanism known as “core–shell” reaction within layered oxides  $\text{NaNiO}_2$  during the initial (de)sodiation processes (Fig. 10a).<sup>215</sup> The integration of quantification analysis with TXM-XANES mappings enabled us to confirm the composition of the irreversible phase formed at a high cut-off voltage of 4.5 V as  $x = 0.17$  in  $\text{Na}_x\text{NiO}_2$ . Our *operando* TXM technique provided

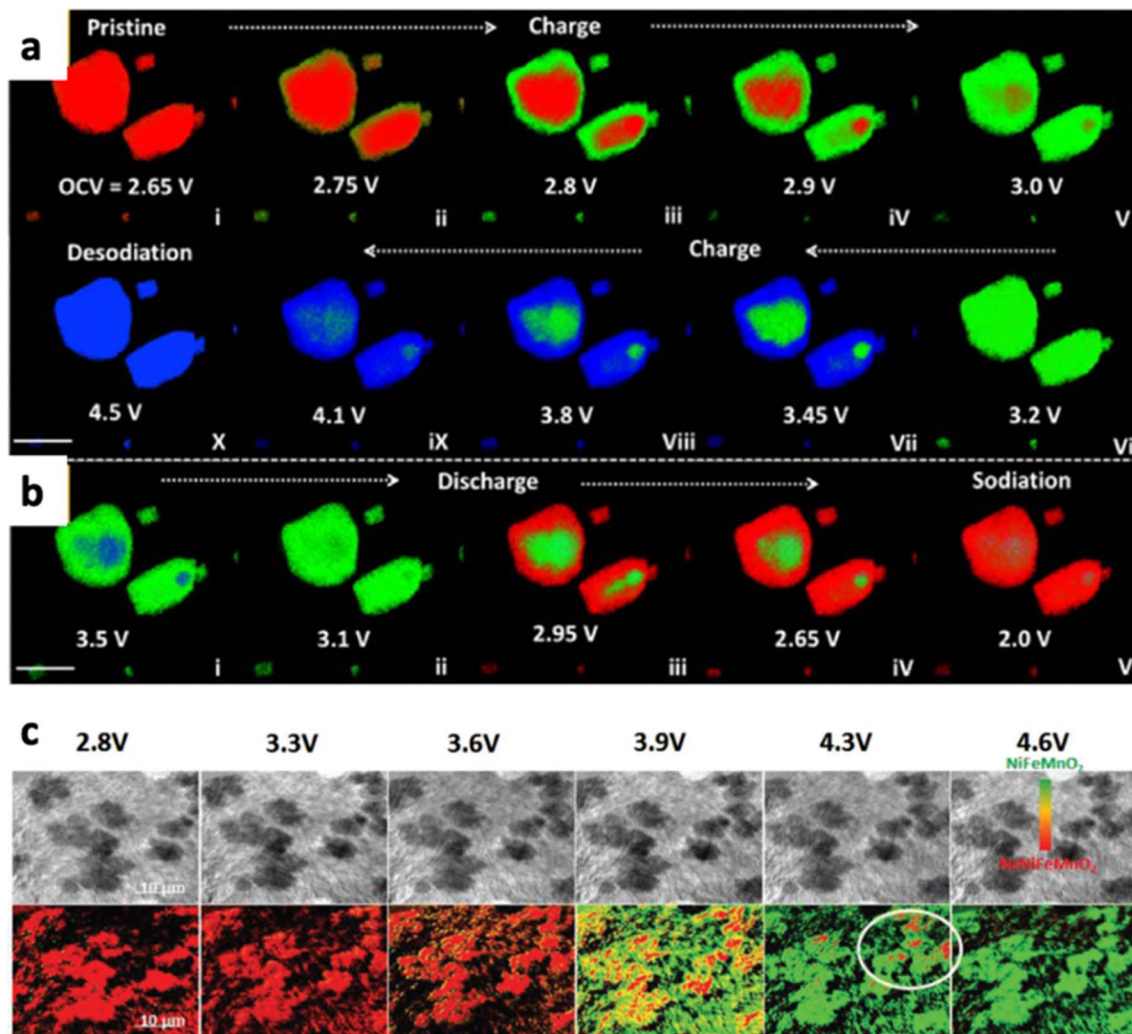


Fig. 10 Operando TXM-XANES results. Chemical phase mappings of NaNiO<sub>2</sub> during (a) the initial charge and (b) discharge processes.<sup>215</sup> (c) TXM image and chemical phase mappings of Na<sub>1-d</sub>Ni<sub>1/3</sub>Fe<sub>1/3</sub>Mn<sub>1/3</sub>O<sub>2</sub> during the initial charge. Reproduced from ref. 216 with permission from Wiley-VCH GmbH, copyright 2016.

insight into relatively sluggish reaction kinetics coupled with irreversible phase transitions, pinpointing the root cause of the initial substantial capacity loss. In another exploration, we examined the ternary layered oxides (NaNi<sub>1/3</sub>Fe<sub>1/3</sub>Mn<sub>1/3</sub>O<sub>2</sub>) and revealed a substitutional solid solution reaction mechanism prevailing in the Na-poor range. Our *operando* TXM-XANES mappings further unveiled several mixed-phase regions existing at various charging states (Fig. 10b).<sup>191</sup> These findings underscore the profound impacts of TXM-XANES as a valuable tool that not only elucidates the complexities of electrochemical reactions but also guides the design of improved battery materials and electrode configurations.

### 5.7. Other characterization techniques

In the realm of advanced battery materials characterized by intricate morphology and unique structural features, conventional analytical techniques may often prove inadequate in elucidating the underlying intricate electrochemical mechanisms. To address these challenges, innovative research

paradigms and cutting-edge techniques have emerged, geared towards unraveling these complexities and advancing our comprehension. These novel approaches serve as a bridge between the complexity of advanced materials and our quest for deeper insights into their behavior. By embracing these progressive methodologies, researchers can navigate the intricacies of these materials and pave the way for breakthroughs in understanding, ultimately propelling the development of next-generation energy storage systems.

A pioneering optical microscopy-based platform was ingeniously employed for the *in situ* investigation and comparative analysis of Li and Na ion transport properties within a singular nanowire structure, as shown in Fig. 11.<sup>217</sup> Notably, a discernible trend emerged, indicating that the conductivity degradation induced by Na<sup>+</sup> ion intercalation surpassed that observed in Li<sup>+</sup> ion system, particularly in the second configuration where only a fraction of the nanowire remained exposed to the electrolyte. This intriguing observation undergoes the more pronounced deterioration in the case of Na<sup>+</sup> ions, hinting at a higher degree of

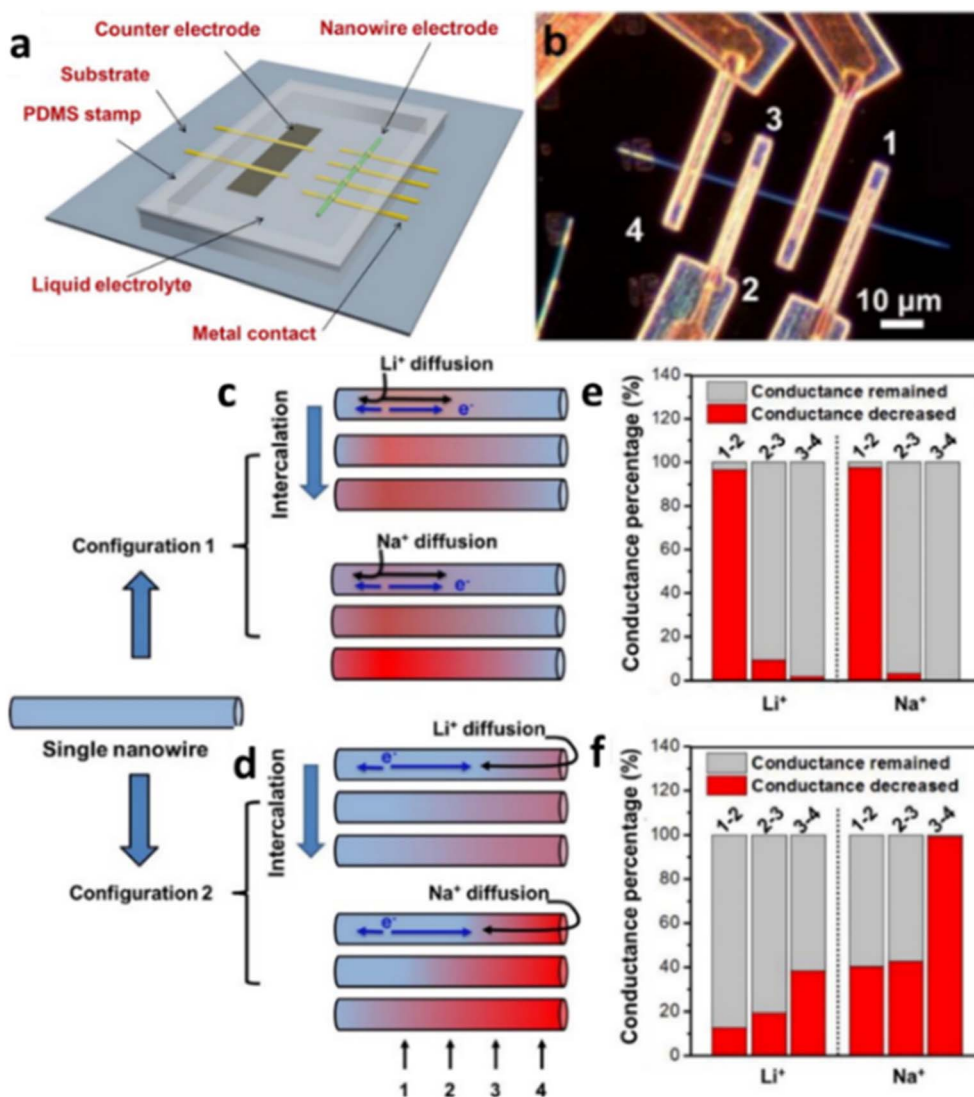


Fig. 11 (a) The overview of the device. (b) The dark field optical microscopic image of the nanowire electrode. Schematic illustration and conductivity retentions of three sections after reaction with Li and Na. (c and d) The conductivity properties of various Sections 1–4 after cycling with Li and Na ions for (e) configuration 1 and (f) configuration 2, respectively. Reproduced from ref. 217 with permission from American Chemical Society, copyright 2015.

degradation compared to their Li<sup>+</sup> counterparts during electrochemical processes. In the layered structure of the H<sub>2</sub>V<sub>3</sub>O<sub>8</sub> nanowire, both Li<sup>+</sup> or Na<sup>+</sup> ions predominantly navigate through the interstitial spaces amidst the stacked layers along *a* axis. Interestingly, analogous behavior is observed when the charge carriers are either Li<sup>+</sup> and Na<sup>+</sup> ions, suggesting a shared electrochemical reaction mechanism within layered electrodes for both lithium and sodium chemistry. However, a crucial disparity comes to light – the crystal structure degradation induced by Na ions is notably more severe than that initiated by Li ions during electrochemical processes. This discrepancy can be attributed to the substantially larger volume of Na ions and the attendant higher energy barrier encountered within the confined interlayer spaces, leading to their more pronounced impact on the crystal structure.

We have compiled an overview of the prominent *operando/in situ* and *ex situ* techniques that have been instrumental in the exploration of cathode materials for SIBs. It is worth noting that there are additional noteworthy *in situ/operando* and *ex situ* techniques, including transmission X-ray microscopy (TXM),<sup>215,218,219</sup> Bragg coherent X-ray diffraction imaging (BCDI),<sup>220,221</sup> etc. These methods have found utility in systems involving lithium and certain anode for SIBs, yet their application to cathode materials in the sodium systems remains relatively uncharted territory. Furthermore, it is pertinent to mention that the realm of *in situ* methods in LIBs research has also received comprehensive attention.<sup>222,223</sup> This underscores the evolving landscape of research methodologies that continue to shape our understanding of energy storage materials.

Characterization techniques possess their own distinctive advantages and application limitations. Among these, *in situ*

XAS can study the local atomic or electronic structure of sodium-ion battery electrode materials in real-time. *In situ* TXM can reveal the heterogeneity of the material's reaction and the spatial distribution of metal elements at the scale of tens of nanometers. *In situ* XRD can explore the average structural transformations of the bulk material, which is particularly necessary for materials based on multi-phase transition reaction mechanisms. *In situ* TEM has significant advantages in the real-time detection of material morphology, phase transitions, and quantification of volume changes. However, *in situ* XRD has limitations in characterizing non-crystalline materials, and the restricted resolution of *in situ* TXM prevents its observation at the atomic scale. Therefore, it is necessary to combine other techniques to compensate for these shortcomings. To more reliably and comprehensively explain the electrochemical phenomena of SIBs, different *in situ* and *operando* characteristic techniques are supposed to consider combining. High-resolution TEM excels in probing nanomaterials at the atomic or nanoscale, but it usually only reveals local information. TXM-based characterization enables the investigation of material behavior at scales from tens of nanometers to tens of micrometers, thereby supplementing the local results of TEM better. Furthermore, by incorporating *in situ* XRD information on crystal structure evolution and *in situ* XAS data on changes in local chemical environments, the integration of these diverse characterization methods significantly enhances our understanding and knowledge of the sodium storage mechanisms in cathode materials. Indeed, this is the case, as more and more researches are now combining two or even more advanced *in situ* testing techniques to systematically investigate the electrochemical behavior of sodium-ion batteries.

## 6. Computation studies of Na ion mobility

A comprehensive review has adeptly consolidated the formidable capabilities of computational methodologies in delving into the intricate atomic-level characteristics of positive electrode materials designed for alkali ion batteries.<sup>224</sup> In broad strokes, the analytical landscape largely comprises two predominant categories of techniques: those rooted in interatomic potential-based methodologies, and those leveraging electronic structure techniques, with density functional theory (DFT) standing out as a prominent representative.

To elucidate the intricacies of diffusion mechanisms within P2 sodium layered oxide materials, researchers harnessed the power of *ab initio* molecular dynamics simulations and the nudged elastic band (NEB) calculations.<sup>225</sup> Their comprehensive exploration has unveiled compelling insights. The outcomes unveil a common thread: both P2 and O3 phases exhibit commendable sodium conductivities, spanning a wide array of sodium concentrations. However, P2-type materials take center stage, boasting higher conductivity compared to O3-type counterparts, barring the domain of high sodium concentrations. In the context of P2 diffusion, a mesmerizing narrative unfolds – a two-dimensional honeycomb lattice pattern is brought to life,

intertwining diverse Na sites. Within this intricate arrangement, Na1 and Na2 sites synchronize in an alternating dance. The exquisite choreography of sodium movement within this honeycomb sublattice, illustrated in Fig. 12a, emerges as a stark departure from diffusion dynamics observed in O3-type materials.

By substituting low-valence cations (Li) in Na layered oxides, the electronic and crystal structures of the oxide cathode  $\text{Na}_x\text{-Cu}_{0.11}\text{Ni}_{0.11}\text{Fe}_{0.3}\text{Mn}_{0.48}\text{O}_2$  (CNFM) were modulated, resulting in the stable synthesis of the high-entropy oxide  $\text{Na}_{0.89}\text{Li}_{0.05}\text{-Cu}_{0.11}\text{Ni}_{0.11}\text{Fe}_{0.3}\text{Mn}_{0.43}\text{O}_{1.97}\text{F}_{0.03}$  (LCNFMF) cathode material. This substitution increases the ratio of  $\text{Na}^+$  content to the available charge transfer number (ACTN) of transition metals (TMs) compared to that of CNFM. First-principles calculations indicated that the substitution of low-valence  $\text{Li}^+$  ions Na layered oxides upshift of the Mn 3d band center. Additionally, the substitution of  $\text{F}^-$  alleviates the increased covalency of the TM–O bond, which results from the significant elevation of the valence state of TMs in the charged state. This, in turn, contributes to improved structural reversibility.<sup>227</sup>

A transformative exploration ensued, orchestrated through the DFT method, to uncover the enigmatic phase transition from P2 to O2. Anchored in the realm of quantum mechanics, the NEB methodology was harnessed to unravel the intricacies of activation barriers within the  $\text{Na}_x[\text{Ni}_{1/2}\text{Mn}_{2/3}]\text{O}_2$  matrix. Within the P2 structure, a captivating Na-ion path – adorned with minimal energy signatures – unveils itself, meandering through the shared face connecting two proximal Na prismatic sites (Fig. 12b).<sup>226</sup> However, an intriguing twist emerges as the Na-ions navigate the terrain: traversing the tetrahedral junction between two octahedral sites, facilitated by the dextrous divacancy mechanism.<sup>228</sup> Notably, the diffusion journey necessitates a mere 170 meV of energy activation. This remarkable feat materializes within the concentration range of 1/3 to 2/3, exhibiting a palpable contrast with its O3-Li counterpart (Fig. 12c and d). The calculated energy threshold positions this P2-type compound in a favorable light, forecasting a higher  $\text{Na}^+$  diffusivity in comparison to the O3-type Li compound – a noteworthy revelation.<sup>227</sup>

Indeed, computational techniques have proven indispensable in the study of various sodium-based polyanion compounds.<sup>229–232</sup> In a noteworthy effort, researchers compared the intercalation behaviors of Na-ion and Li-ion compounds by delving into three crucial battery attributes: voltage, phase stability, and diffusion barriers.<sup>226</sup> Their calculations unveiled that the voltages associated with Na-based compounds are lower by 0.18–0.57 V compared to their corresponding Li-ion counterparts (Fig. 12e). This phenomenon, attributed to a cathodic effect, can be linked to the lesser energy gain from sodium insertion into the host structure as opposed to lithium insertion. Delving further into phase stability, it was observed that open structures like layered and NASICON structures, which can better accommodate the larger  $\text{Na}^+$  ions, commonly offer both Na and Li versions of the same compound. In contrast, within closed-packed AMPO<sub>4</sub> structures, lithium favors the olivine structure, while sodium predominantly prefers the maricite structure, aligning with earlier

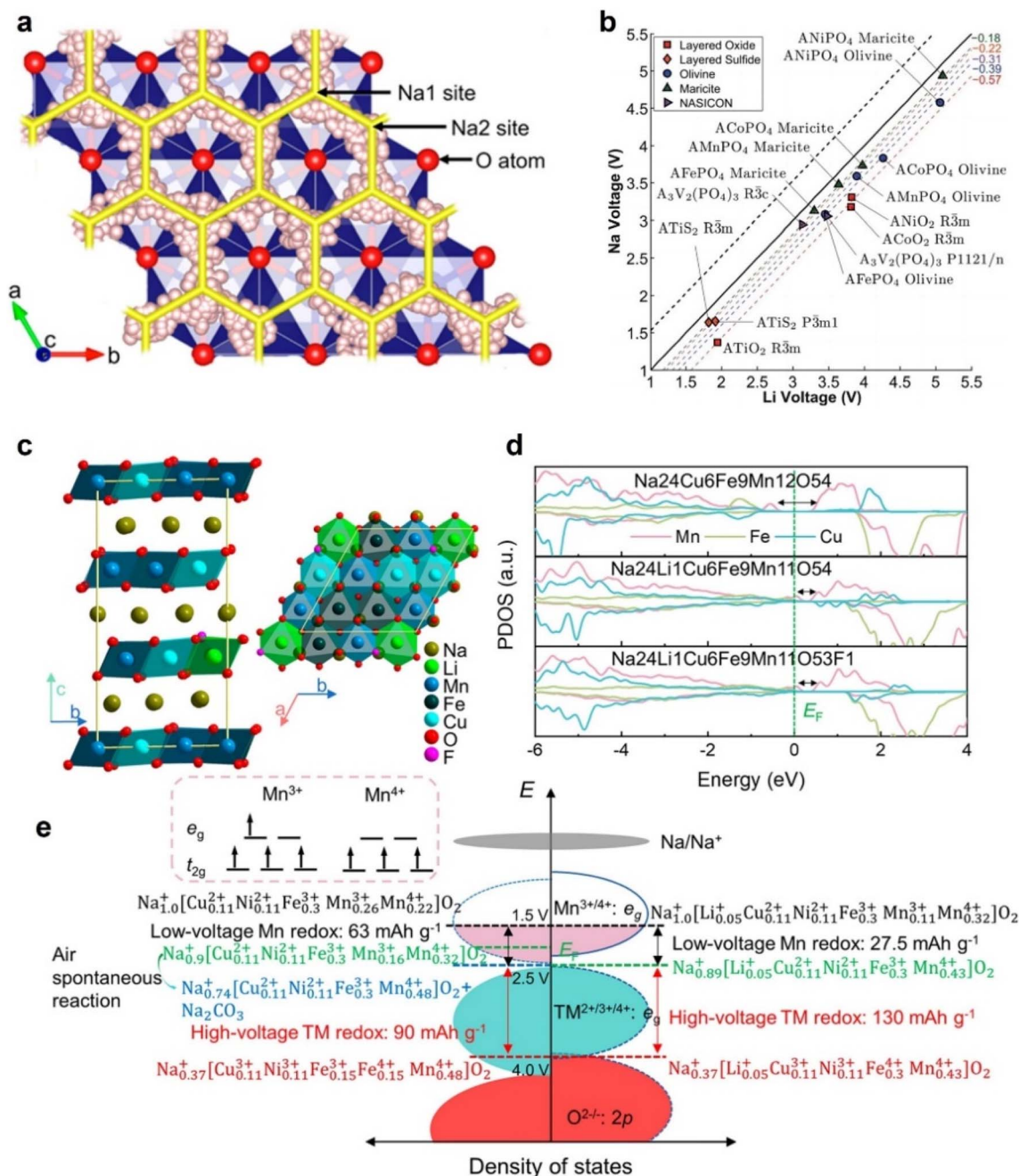


**Fig. 12** (a) Na ions diffusion pathways in P2  $\text{Na}_{0.56}\text{CoO}_2$ . Reproduced from ref. 225 with permission from American Chemical Society, copyright 2014. (b) Comparison of Na voltage vs. Li voltage for different structures obtained by theoretical calculations. Reproduced from ref. 226 with permission from the Royal Society of Chemistry, copyright 2011. (c) Crystal structure of  $\text{Na}_{24}\text{Li}_1\text{Cu}_6\text{Fe}_9\text{Mn}_{11}\text{O}_{53}\text{F}_1$ . (d) Calculated projected density of states for transition metals in  $\text{Na}_{24}\text{Cu}_6\text{Fe}_9\text{Mn}_{12}\text{O}_{54}$ ,  $\text{Na}_{24}\text{Li}_1\text{Cu}_6\text{Fe}_9\text{Mn}_{11}\text{O}_{54}$ , and  $\text{Na}_{24}\text{Li}_1\text{Cu}_6\text{Fe}_9\text{Mn}_{11}\text{O}_{53}\text{F}_1$ . (e) Schematic diagram of the electronic structure adjustment of CNFM and LCNFM,  $E_F$ : Fermi level. Dotted box: electronic occupancy in the 3d orbitals of  $\text{Mn}^{3+}$  and  $\text{Mn}^{4+}$ . Reproduced from ref. 227 with permission from American Chemical Society, copyright 2023.

experimental observations. Intriguingly, the computational analyses indicated that the barriers governing  $\text{Na}^+$  migration could potentially be lower than those for  $\text{Li}^+$  migration in the context of layered structures.<sup>226</sup> Additionally, first-principle calculations hinted at the possibility of Na-vacancy ordering within Na-intercalation compounds, both layered structures and polyanionic compounds. This ordering could potentially

give rise to the formation of stable intermediate phases, leading to distinct electrochemical mechanisms that diverge from conventional expectations.<sup>77,193</sup>

Incorporating potential-based methods, a study was conducted to contrast the Na conduction characteristics of olivine-type  $\text{NaMPO}_4$  ( $M = \text{Fe}, \text{Mn}$ ) with layer-structured  $\text{Na}_2\text{FePO}_4\text{F}$  (Fig. 12f-i).<sup>233</sup> Within the olivine framework, the migration of

sodium ion is primarily confined to the [010] direction, following a curved trajectory akin to  $\text{LiMPO}_4$ . However, this migration entails a lower energy barrier of 0.3 eV. Conversely, in  $\text{Na}_2\text{FePO}_4\text{F}$ ,  $\text{Na}^+$  ion conduction is envisaged as a two-dimensional network residing within the *ac* plane of the orthorhombic *Pnma* structure, offering a comparably low activation energy (Fig. 12f–i). The findings also underscore the paramount significance of volume expansion-induced strain during the process of (de)intercalation, a phenomenon that is more pronounced for the relatively larger  $\text{Na}^+$  ions in comparison to  $\text{Li}^+$ . This notion delineates that materials with substantial volume discrepancies between their end member phases are inclined to exhibit inadequate rate capacity and quicker capacity degradation.

## 7. Summary and outlook

In recent years, SIBs have garnered significant attention as a promising energy storage technology. While their energy density typically falls short of that achieved by lithium-ion batteries (LIBs), SIBs exhibit certain advantages that position them as competitive alternatives, particularly in domains such as large-scale electricity storage and smart grid applications. These advantages primarily stem from their inherent cost-effectiveness, which renders them particularly suitable for cost-driven scenarios. However, it is important to acknowledge that despite their potential, the commercial viability of sodium-ion batteries is not without its formidable challenges. Several critical issues must be addressed to fully realize their practical implementation. These challenges can be succinctly outlined as follows:

(i) New materials. The current landscape of cathode materials for SIBs presents a series of challenges. Layered transition-metal oxides exhibit high specific capacities, operational voltages, and extended cycle lives exceeding 1000 cycles. However, they still face several key challenges, such as irreversible phase transitions and excessive reactivity to moisture; polyanionic compounds show high operating voltages and structural stability. However, they are compromised by their limited ionic and electronic conductivities, as well as a reduction in specific capacity due to their large molecular structures; PBAs are capable of achieving high energy densities and can be synthesized at relatively low temperatures. Nevertheless, their synthesis in aqueous media typically results in the incorporation of coordinated or interstitial water, leading to an accumulation of capacity loss. To address these issues, researchers are compelled to explore multifaceted solutions. On one hand, the scientific community must devise strategies to mitigate the aforementioned problems by developing effective protective measures against air reactivity, enhancing voltage plateaus, and optimizing overall electrochemical stability. On the other hand, there is a pressing need to identify novel materials that boast innovative structural attributes. These materials should not only enhance energy density, but also facilitate swifter charge-discharge rates and protracted cycle life, thereby pushing the envelope of sodium-ion battery performance to new heights.

(ii) Synthesis methods. While many synthesis methods applicable to LIBs electrode materials can be adapted for sodium-based materials, certain cathode materials, like olivine  $\text{NaMPO}_4$  ( $M = \text{Fe}, \text{Mn}, \text{etc.}$ ), pose unique challenges that necessitate fresh approaches. These distinct materials cannot be readily synthesized using conventional methods tailored for LIB cathode materials. Consequently, there is a compelling need to innovate and develop novel synthesis techniques to effectively address the specific demands of sodium-ion battery materials. These advanced methods should be tailored to accommodate the novel structures and morphologies of emerging materials, thereby fostering enhanced capabilities for sodium-ion batteries. By spearheading the development of innovative synthesis strategies, researchers can unlock new horizons for material design and performance optimization in the realm of sodium-ion batteries.

(iii) *Operando/in situ* measurements. The utilization of and *in situ* measurement techniques holds paramount significance in advancing the comprehension of battery materials, be it for lithium-ion batteries or sodium-ion batteries. Over the recent years, a plethora of methods have been cultivated to probe the intricacies of battery materials, encompassing *in situ* transmission electron microscopy (TEM), *in situ* transmission X-ray microscopy (TXM), and *in situ* X-ray tomography. Notably, these techniques have predominantly been employed in the study of lithium-ion battery materials, with their application in cathode materials for sodium-ion batteries still relatively limited. Of particular note are *in situ* TXM and X-ray tomography techniques, which offer real-time imaging capabilities endowed with both temporal and spatial resolution precision. These innovative methodologies provide the unique advantage of furnishing dynamic insights into the structural dynamics and chemical composition of battery materials during cycling. To expedite the progress of sodium-ion battery research, further exploration and deployment of these advanced *operando* and *in situ* measurement techniques, particularly within the domain of cathode materials, are imperative. This concerted effort will undoubtedly contribute to unveiling hitherto unexplored facets of battery behavior and performance, thereby catalyzing advancements in sodium-ion battery technology.

(iv) Simulation techniques. The synergy between experimental and computational methodologies presents a formidable avenue for expediting the discovery and characterization of electrode materials, alongside fostering an enhanced comprehension of the intricate structural evolution mechanisms during charge-discharge processes. The realm of computational modeling is pivotal in prognosticating and designing novel electrode materials, amplifying the analysis of experimental findings, and facilitating an intrinsic understanding of evolutionary phenomena that might elude conventional experimental approaches alone. This symbiotic interplay between experimental and computational domains holds the promise of unraveling unprecedented insights, ultimately propelling advancements in electrode material science. As such, the integration of simulation techniques with empirical investigations stands poised to foster an enriched

understanding of battery materials and catalyze the development of high-performance sodium-ion battery systems.

## Data availability

No primary research results, software or code have been included and no new data were generated or analysed as part of this review.

## Conflicts of interest

There are no conflicts to declare.

## Acknowledgements

This work was supported by National Natural Science Foundation of China (52272241, 52107223), Zhejiang Provincial Natural Science Foundation of China (No. LR24E020001), and Talent Introduction of Chongqing University of Science and Technology (ckrc2022046).

## References

- B. Dunn, H. Kamath and J. M. Tarascon, *Science*, 2011, **334**, 928–935.
- R. Usiskin, Y. Lu, J. Popovic, M. Law, P. Balaya, Y.-S. Hu and J. Maier, *Nat. Rev. Mater.*, 2021, **6**, 1020–1035.
- S. Chu, S. Guo and H. Zhou, *Chem. Soc. Rev.*, 2021, **50**, 13189–13235.
- P. Gupta, S. Pushpakanth, M. A. Haider and S. Basu, *ACS Omega*, 2022, **7**, 5605–5614.
- J. Barandiarán, *World Dev.*, 2019, **113**, 381–391.
- F. Risacher and B. Fritz, *Aquat. Geochem.*, 2008, **15**, 123–157.
- A. Yaksic and J. E. Tilton, *Resour. Policy*, 2009, **34**, 185–194.
- B. Senthilkumar, C. Murugesan, L. Sharma, S. Lochab and P. Barpanda, *Small Methods*, 2018, **3**, 1800253.
- R. D. Shannon, *Acta Crystallogr.*, 1976, **32**, 751–767.
- H. L. Pan, Y. S. Hu and L. Q. Chen, *Energy Environ. Sci.*, 2013, **6**, 2338–2360.
- R. Usiskin, Y. Lu, J. Popovic, M. Law, P. Balaya, Y.-S. Hu and J. Maier, *Nat. Rev. Mater.*, 2021, **6**, 1020–1035.
- W. Zuo and Y. Yang, *Acc. Mater. Res.*, 2022, **3**, 709–720.
- A. Rudola, R. Sayers, C. J. Wright and J. Barker, *Nat. Energy*, 2023, **8**, 215–218.
- E. Goikolea, V. Palomares, S. Wang, I. R. Larramendi, X. Guo, G. Wang and T. Rojo, *Adv. Energy Mater.*, 2020, **10**, 2002055.
- X. H. Liu, J. Peng, W. H. Lai, Y. Gao, H. Zhang, L. Li, Y. Qiao and S. L. Chou, *Adv. Funct. Mater.*, 2021, 2108616.
- Z. Hao, X. Shi, Z. Yang, X. Zhou, L. Li, C.-Q. Ma and S. Chou, *Adv. Mater.*, 2023, **36**, 2305135.
- M. Chen, Q. Liu, S. W. Wang, E. Wang, X. Guo and S. L. Chou, *Adv. Energy Mater.*, 2019, **9**, 1803609.
- W. Zuo, A. Innocenti, M. Zarrabeitia, D. Bresser, Y. Yang and S. Passerini, *Acc. Chem. Res.*, 2023, **56**, 284–296.
- J. Chen, G. Adit, L. Li, Y. Zhang, D. H. C. Chua and P. S. Lee, *Energy Environ. Mater.*, 2023, **6**, e12633.
- X. Liang, J.-Y. Hwang and Y.-K. Sun, *Adv. Energy Mater.*, 2023, **13**, 2301975.
- Z. Tian, Y. Zhang, J. Zhu, Q. Li, T. Liu and M. Antonietti, *Adv. Energy Mater.*, 2021, **11**, 2102489.
- K. Wang, H. Zhuo, J. Wang, F. Poon, X. Sun and B. Xiao, *Adv. Funct. Mater.*, 2023, **33**, 2212607.
- H. Yao, H. Li, B. Ke, S. Chu, S. Guo and H. Zhou, *Small Methods*, 2023, **7**, 2201555.
- F. Li, R. Liu, J. Liu and H. Li, *Adv. Funct. Mater.*, 2023, **33**, 2300602.
- Y.-F. Liu, K. Han, D.-N. Peng, L.-Y. Kong, Y. Su, H.-W. Li, H.-Y. Hu, J.-Y. Li, H.-R. Wang, Z.-Q. Fu, Q. Ma, Y.-F. Zhu, R.-R. Tang, S.-L. Chou, Y. Xiao and X.-W. Wu, *InfoMat*, 2023, **5**, e12422.
- N. Yabuuchi, K. Kubota, M. Dahbi and S. Komaba, *Chem. Rev.*, 2014, **114**, 11636–11682.
- M. S. Islam and C. A. Fisher, *Chem. Soc. Rev.*, 2014, **43**, 185–204.
- D. Kundu, E. Talaie, V. Duffort and L. F. Nazar, *Angew. Chem.*, 2015, **54**, 3431–3448.
- M. D. Slater, D. Kim, E. Lee and C. S. Johnson, *Adv. Funct. Mater.*, 2013, **23**, 947–958.
- S. W. Kim, D. H. Seo, X. H. Ma, G. Ceder and K. Kang, *Adv. Energy Mater.*, 2012, **2**, 710–721.
- M. H. Han, E. Gonzalo, G. Singh and T. Rojo, *Energy Environ. Sci.*, 2015, **8**, 81–102.
- K. Kubota, N. Yabuuchi, H. Yoshida, M. Dahbi and S. Komaba, *MRS Bull.*, 2014, **39**, 416–422.
- C. Delmas, D. Carlier and M. Guignard, *Adv. Energy Mater.*, 2020, **11**, 2001201.
- T. Jin, H. Li, K. Zhu, P. F. Wang, P. Liu and L. Jiao, *Chem. Soc. Rev.*, 2020, **49**, 2342–2377.
- R.-M. Gao, Z.-J. Zheng, P.-F. Wang, C.-Y. Wang, H. Ye and F.-F. Cao, *Energy Storage Mater.*, 2020, **30**, 9–26.
- G. Du and H. Pang, *Energy Storage Mater.*, 2021, **36**, 387–408.
- X. Wu, Y. Ru, Y. Bai, G. Zhang, Y. Shi and H. Pang, *Coord. Chem. Rev.*, 2022, **451**, 214260.
- J. Chen, L. Wei, A. Mahmood, Z. Pei, Z. Zhou, X. Chen and Y. Chen, *Energy Storage Mater.*, 2020, **25**, 585–612.
- F. Wei, Q. Zhang, P. Zhang, W. Tian, K. Dai, L. Zhang, J. Mao and G. Shao, *J. Electrochem. Soc.*, 2021, **168**, 050524.
- Q. Liu, Z. Hu, W. Li, C. Zou, H. Jin, S. Wang, S. Chou and S.-X. Dou, *Energy Environ. Sci.*, 2021, **14**, 158–179.
- Q. Liu, Z. Hu, M. Chen, C. Zou, H. Jin, S. Wang, S. L. Chou, Y. Liu and S. X. Dou, *Adv. Funct. Mater.*, 2020, 1909530.
- Y. Xiao, N. M. Abbasi, Y. F. Zhu, S. Li, S. J. Tan, W. Ling, L. Peng, T. Yang, L. Wang, X. D. Guo, Y. X. Yin, H. Zhang and Y. G. Guo, *Adv. Funct. Mater.*, 2020, **30**, 2001334.
- S. Y. Zhang, Y. J. Guo, Y. N. Zhou, X. D. Zhang, Y. B. Niu, E. H. Wang, L. B. Huang, P. F. An, J. Zhang, X. A. Yang, Y. X. Yin, S. Xu and Y. G. Guo, *Small*, 2021, **17**, e2007236.
- J. Song, K. Wang, J. Zheng, M. H. Engelhard, B. Xiao, E. Hu, Z. Zhu, C. Wang, M. Sui, Y. Lin, D. Reed, V. L. Sprenkle, P. Yan and X. Li, *ACS Energy Lett.*, 2020, **5**, 1718–1725.

- 45 J. C. Kim, D. H. Kwon, J. H. Yang, H. Kim, S. H. Bo, L. Wu, H. Kim, D. H. Seo, T. Shi, J. Wang, Y. Zhu and G. Ceder, *Adv. Energy Mater.*, 2020, **10**, 2001151.
- 46 Y. Shi, Z. Zhang, P. Jiang, A. Gao, K. Li, Q. Zhang, Y. Sun, X. Lu, D. Cao and X. Lu, *Energy Storage Mater.*, 2021, **37**, 354–362.
- 47 C. Zhao, Q. Wang, Z. Yao, J. Wang, B. Sánchez-Lengeling, F. Ding, X. Qi, Y. Lu, X. Bai, B. Li, H. Li, A. Aspuru-Guzik, X. Huang, C. Delmas, M. Wagemaker, L. Chen and Y.-S. Hu, *Science*, 2020, **370**, 708–711.
- 48 C. Delmas, C. Fouassier and P. Hagenmuller, *Physica*, 1980, **99**, 81–85.
- 49 Z. Jian, L. Zhao, H. Pan, Y.-S. Hu, H. Li, W. Chen and L. Chen, *Electrochem. Commun.*, 2012, **14**, 86–89.
- 50 P. Moreau, D. Guyomard, J. Gaubicher and F. Boucher, *Chem. Mater.*, 2010, **22**, 4126–4128.
- 51 Q. Wang, H. Gao, J. Li, G. B. Liu and H. Jin, *ACS Appl. Mater. Interfaces*, 2021, **13**, 14312–14320.
- 52 K. Liang, S. Wang, H. Zhao, X. Huang, Y. Ren, Z. He, J. Mao and J. Zheng, *Chem. Eng. J.*, 2022, **428**, 131780.
- 53 Z. Yang, G. Li, J. Sun, L. Xie, Y. Jiang, Y. Huang and S. Chen, *Energy Storage Mater.*, 2020, **25**, 724–730.
- 54 L. Deng, F.-D. Yu, Y. Xia, Y.-S. Jiang, X.-L. Sui, L. Zhao, X.-H. Meng, L.-F. Que and Z.-B. Wang, *Nano Energy*, 2021, **82**, 105659.
- 55 P. Barpanda, G. Oyama, S. Nishimura, S. C. Chung and A. Yamada, *Nat. Commun.*, 2014, **5**, 4358.
- 56 A. Plewa, A. Kulka, E. Hanc, W. Zając, J. Sun, L. Lu and J. Molenda, *J. Mater. Chem. A*, 2020, **8**, 2728–2740.
- 57 H. Zhang, X. Tan, H. Li, S. Passerini and W. Huang, *Energy Environ. Sci.*, 2021, **14**, 5788–5800.
- 58 P. Zuo, L. Wang, W. Zhang, G. Yin, Y. Ma, C. Du, X. Cheng and Y. Gao, *Nanoscale*, 2015, **7**, 11509–11514.
- 59 H. Fei, X. Liu, Y. Lin and M. Wei, *J. Colloid Interface Sci.*, 2014, **428**, 73–77.
- 60 M. Galceran, V. Roddatis, F. J. Zúñiga, J. M. Pérez-Mato, B. Acebedo, R. Arenal, I. Peral, T. Rojo and M. Casas-Cabanas, *Chem. Mater.*, 2014, **26**, 3289–3294.
- 61 M. Casas-Cabanas, V. V. Roddatis, D. Saurel, P. Kubiak, J. Carretero-Gonzalez, V. Palomares, P. Serras and T. Rojo, *J. Mater. Chem.*, 2012, **22**, 17421–17423.
- 62 J. B. Goodenough, H. Y.-P. Hong and J. A. Kafalas, *Mater. Res. Bull.*, 1976, **11**, 203–220.
- 63 A. K. Padhi, K. S. Nanjundaswamy, C. Masquelier and J. B. Goodenough, *J. Electrochem. Soc.*, 1997, **144**, 2581–2586.
- 64 H. Huang, S.-C. Yin, T. Kerr, N. Taylor and L. F. Nazar, *Adv. Mater.*, 2002, **14**, 1525–1528.
- 65 X. Min, H. Huo, R. Li, J. Zhou, Y. Hu and C. Dai, *J. Electroanal. Chem.*, 2016, **774**, 76–82.
- 66 K. Saravanan, C. W. Mason, A. Rudola, K. H. Wong and P. Balaya, *Adv. Energy Mater.*, 2013, **3**, 444–450.
- 67 Y. Lu, L. Wang, J. Cheng and J. B. Goodenough, *Chem. Commun.*, 2012, **48**, 6544–6546.
- 68 H. Yi, R. Qin, S. Ding, Y. Wang, S. Li, Q. Zhao and F. Pan, *Adv. Funct. Mater.*, 2020, 2006970.
- 69 J. Qian, C. Wu, Y. Cao, Z. Ma, Y. Huang, X. Ai and H. Yang, *Adv. Energy Mater.*, 2018, **8**, 1702619.
- 70 F. Feng, S. Chen, S. Zhao, W. Zhang, Y. Miao, H. Che, X.-Z. Liao and Z.-F. Ma, *Chem. Eng. J.*, 2021, **411**, 128518.
- 71 Y. Tang, W. Li, P. Feng, M. Zhou, K. Wang, Y. Wang, K. Zaghbi and K. Jiang, *Adv. Funct. Mater.*, 2020, **30**, 1908754.
- 72 J. Peng, W. Zhang, Z. Hu, L. Zhao, C. Wu, G. Peleckis, Q. Gu, J. Z. Wang, H. K. Liu, S. X. Dou and S. Chou, *Nano Lett.*, 2022, **22**, 1302–1310.
- 73 H. J. Buser, D. Schwarzenbach, W. Petter and A. Ludi, *Inorg. Chem.*, 1977, **16**, 2704–2710.
- 74 Y. Yue, A. J. Binder, B. Guo, Z. Zhang, Z.-A. Qiao, C. Tian and S. Dai, *Angew. Chem., Int. Ed.*, 2014, **53**, 3134–3137.
- 75 C. D. Wessells, S. V. Peddada, M. T. McDowell, R. A. Huggins and Y. Cui, *J. Electrochem. Soc.*, 2012, **159**, A98.
- 76 Y. Mizuno, M. Okubo, E. Hosono, T. Kudo, H. Zhou and K. Oh-ishi, *J. Phys. Chem. C*, 2013, **117**, 10877–10882.
- 77 R. Berthelot, D. Carlier and C. Delmas, *Nat. Mater.*, 2011, **10**, 74–80.
- 78 T. Ohzuku and A. Ueda, *J. Electrochem. Soc.*, 1994, **141**, 2972–2977.
- 79 J. Reed, G. Ceder and A. Van Der Ven, *Electrochem. Solid-State Lett.*, 2001, **4**, A78.
- 80 X. Li, Y. Wang, D. Wu, L. Liu, S.-H. Bo and G. Ceder, *Chem. Mater.*, 2016, **28**, 6575–6583.
- 81 C. Sun, Q. Ni, M. Li, Z. Sun, X. Yuan, L. Li, K. Wang, H. Jin and Y. Zhao, *Adv. Funct. Mater.*, 2024, **34**, 2310248.
- 82 A. Mendiboure, C. Delmas and P. Hagenmuller, *J. Solid State Chem.*, 1985, **57**, 323–331.
- 83 O. I. Velikokhatnyi, C. C. Chang and P. N. Kumta, *J. Electrochem. Soc.*, 2003, **150**, A1262.
- 84 C. Delmas, J. J. Braconnier, C. Fouassier and P. Hagenmuller, *Solid State Ionics*, 1981, **3–4**, 165–169.
- 85 J. J. Ding, Y. N. Zhou, Q. Sun, X. Q. Yu, X. Q. Yang and Z. W. Fu, *Electrochim. Acta*, 2013, **87**, 388–393.
- 86 X. Ma, H. Chen and G. Ceder, *J. Electrochem. Soc.*, 2011, **158**, A1307.
- 87 J. Billaud, R. J. Clement, A. R. Armstrong, J. Canales-Vazquez, P. Rozier, C. P. Grey and P. G. Bruce, *J. Am. Chem. Soc.*, 2014, **136**, 17243–17248.
- 88 P. Vassilaras, X. Ma, X. Li and G. Ceder, *J. Electrochem. Soc.*, 2012, **160**, A207–A211.
- 89 S. Yamada, M. Fujiwara and M. Kanda, *J. Power Sources*, 1995, **54**, 209–213.
- 90 M. Guignard, C. Didier, J. Darriet, P. Bordet, E. Elkaim and C. Delmas, *Nat. Mater.*, 2013, **12**, 74–80.
- 91 A. R. Armstrong, C. Lyness, P. M. Panchmatia, M. S. Islam and P. G. Bruce, *Nat. Mater.*, 2011, **10**, 223–229.
- 92 R. Rajapriya and M. S. Dangate, in *Integrated Green Energy Solutions Volume 1*, 2023, pp. 27–44, DOI: [10.1002/9781119847564.ch3](https://doi.org/10.1002/9781119847564.ch3).
- 93 S. Komaba, C. Takei, T. Nakayama, A. Ogata and N. Yabuuchi, *Electrochem. Commun.*, 2010, **12**, 355–358.

- 94 S. Chu, D. Kim, G. Choi, C. Zhang, H. Li, W. K. Pang, Y. Fan, A. M. D'Angelo, S. Guo and H. Zhou, *Angew. Chem., Int. Ed.*, 2023, **62**, e202216174.
- 95 N. Yabuuchi, H. Yoshida and S. Komaba, *Electrochemistry*, 2012, **80**, 716–719.
- 96 N. Yabuuchi, M. Kajiyama, J. Iwatate, H. Nishikawa, S. Hitomi, R. Okuyama, R. Usui, Y. Yamada and S. Komaba, *Nat. Mater.*, 2012, **11**, 512–517.
- 97 D. H. Lee, J. Xu and Y. S. Meng, *Phys. Chem. Chem. Phys.*, 2013, **15**, 3304–3312.
- 98 S. Wu, B. Su, K. Ni, F. Pan, C. Wang, K. Zhang, D. Y. W. Yu, Y. Zhu and W. Zhang, *Adv. Energy Mater.*, 2021, **11**, 2002737.
- 99 P. K. Nayak, J. Grinblat, M. D. Levi, O. Haik, E. Levi, M. Talianker, B. Markovskiy, Y.-K. Sun and D. Aurbach, *Chem. Mater.*, 2015, **27**, 2600–2611.
- 100 L. Zhao, L. Yu, G. Wan, N. Ahmad, X. Ma, Z. Tao and G. Zhang, *Small Sci.*, 2023, **3**, 2300122.
- 101 J. Lu, S. C. Chung, S.-i. Nishimura and A. Yamada, *Chem. Mater.*, 2013, **25**, 4557–4565.
- 102 H. Zhang, L. Wang, L. Ma, Y. Liu, B. Hou, N. Shang, S. Zhang, J. Song, S. Chen and X. Zhao, *Adv. Sci.*, 2024, **11**, 2306168.
- 103 C. Zhu, K. Song, P. A. van Aken, J. Maier and Y. Yu, *Nano Lett.*, 2014, **14**, 2175–2180.
- 104 L. Liang, X. Li, F. Zhao, J. Zhang, Y. Liu, L. Hou and C. Yuan, *Adv. Energy Mater.*, 2021, **11**, 2100287.
- 105 H. Huang, S.-C. Yin, T. Kerr, N. Taylor and L. F. Nazar, *Adv. Mater.*, 2002, **14**, 1525–1528.
- 106 M. Chen, D. Cortie, Z. Hu, H. Jin, S. Wang, Q. Gu, W. Hua, E. Wang, W. Lai, L. Chen, S.-L. Chou, X.-L. Wang and S.-X. Dou, *Adv. Energy Mater.*, 2018, **8**, 1800944.
- 107 L.-L. Zhang, C. Wei, X.-Y. Fu, Z.-Y. Chen, B. Yan, P.-P. Sun, K.-J. Chang and X.-L. Yang, *Carbon Energy*, 2021, **3**, 827–839.
- 108 N. Imanishi, T. Morikawa, J. Kondo, Y. Takeda, O. Yamamoto, N. Kinugasa and T. Yamagishi, *J. Power Sources*, 1999, **79**, 215–219.
- 109 N. Meethong, H. Y. S. Huang, S. A. Speakman, W. C. Carter and Y. M. Chiang, *Adv. Funct. Mater.*, 2007, **17**, 1115–1123.
- 110 W. Paul, *Mater. Res. Bull.*, 1970, **5**, 691–702.
- 111 J. Feinleib and W. Paul, *Phys. Rev.*, 1967, **155**, 841–850.
- 112 M. Onoda, *J. Phys.: Condens. Matter*, 2008, **20**, 145205.
- 113 S. Hartung, N. Bucher, J. B. Franklin, A. M. Wise, L. Y. Lim, H.-Y. Chen, J. N. Weker, M.-E. Michel-Beyerle, M. F. Toney and M. Srinivasan, *Adv. Energy Mater.*, 2016, **6**, 1502336.
- 114 A. Rougier, P. Gravereau and C. Delmas, *J. Electrochem. Soc.*, 1996, **143**, 1168–1175.
- 115 C. Delmas, D. Carlier and M. Guignard, *Adv. Energy Mater.*, 2021, **11**, 2001201.
- 116 H. Chen, J. A. Dawson and J. H. Harding, *J. Mater. Chem. A*, 2014, **2**, 7988–7996.
- 117 J. J. Braconnier, C. Delmas and P. Hagenmuller, *Mater. Res. Bull.*, 1982, **17**, 993–1000.
- 118 J. Liu, W. H. Kan and C. D. Ling, *J. Power Sources*, 2021, **481**, 229139.
- 119 M. H. Han, E. Gonzalo, M. Casas-Cabanas and T. Rojo, *J. Power Sources*, 2014, **258**, 266–271.
- 120 P. Suresh, A. K. Shukla and N. Munichandraiah, *J. Power Sources*, 2006, **159**, 1395–1400.
- 121 J. Kim and A. Manthiram, *J. Electrochem. Soc.*, 1999, **146**, 4371–4374.
- 122 K. Ado, M. Tabuchi, H. Kobayashi, H. Kageyama, O. Nakamura, Y. Inaba, R. Kanno, M. Takagi and Y. Takeda, *J. Electrochem. Soc.*, 1997, **144**, L177–L180.
- 123 Y. Takeda, J. Akagi, A. Edagawa, M. Inagaki and S. Naka, *Mater. Res. Bull.*, 1980, **15**, 1167–1172.
- 124 Y. Takeda, K. Nakahara, M. Nishijima, N. Imanishi, O. Yamamoto and M. Takano, *Mater. Res. Bull.*, 1994, **29**, 659–666.
- 125 E. Lee, D. E. Brown, E. E. Alp, Y. Ren, J. Lu, J.-J. Woo and C. S. Johnson, *Chem. Mater.*, 2015, **27**, 6755–6764.
- 126 C. D. W. Jones, E. Rossen and J. R. Dahn, *Solid State Ionics*, 1994, **68**, 65–69.
- 127 C. Lin, X. Meng, M. Liang, W. Li, J. Liang, T. Liu, X. Ke, J. Liu, Z. Shi and L. Liu, *J. Mater. Chem. A*, 2023, **11**, 68–76.
- 128 I. Lee, G. Oh, S. Lee, T.-Y. Yu, M. H. Alfaruqi, V. Mathew, B. Sambandam, Y.-K. Sun, J.-Y. Hwang and J. Kim, *Energy Storage Mater.*, 2021, **41**, 183–195.
- 129 Y. Lyu, L. Ben, Y. Sun, D. Tang, K. Xu, L. Gu, R. Xiao, H. Li, L. Chen and X. Huang, *J. Power Sources*, 2015, **273**, 1218–1225.
- 130 W. E. Gent, I. I. Abate, W. Yang, L. F. Nazar and W. C. Chueh, *Joule*, 2020, **4**, 1369–1397.
- 131 W. Li, Y. Wang, G. Hu, Z. Peng, Y. Cao, Y. Zeng and K. Du, *J. Alloys Compd.*, 2019, **779**, 147–155.
- 132 C. L. Jakobsen, M. Brighi, B. P. Andersen, G. Ducrest, R. Černý and D. B. Ravnsbæk, *J. Power Sources*, 2022, **535**, 231317.
- 133 C. L. Jakobsen, B. P. Andersen, M. Johansen, C. K. Christensen, A. Ø. Drejer, M. A. Karlsen and D. B. Ravnsbæk, *J. Power Sources*, 2024, **591**, 233875.
- 134 F. Geng, Q. Yang, C. Li, B. Hu, C. Zhao, M. Shen and B. Hu, *J. Phys. Chem. Lett.*, 2021, **12**, 781–786.
- 135 A. K. Padhi, K. S. Nanjundaswamy and J. B. Goodenough, *J. Electrochem. Soc.*, 1997, **144**, 1188–1194.
- 136 T. Flack, S. A. Jobbins, S. E. Boulfelfel and S. Leoni, *J. Phys. Chem. C*, 2022, **126**, 12339–12347.
- 137 J. He, J. Meng and Y. Huang, *J. Power Sources*, 2023, **570**, 232965.
- 138 K. T. Lee, T. N. Ramesh, F. Nan, G. Botton and L. F. Nazar, *Chem. Mater.*, 2011, **23**, 3593–3600.
- 139 L. He, H. Li, X. Ge, S. Li, X. Wang, S. Wang, L. Zhang and Z. Zhang, *Adv. Mater. Interfaces*, 2022, **9**, 2200515.
- 140 W. Yang, Q. Liu, Y. Zhao, D. Mu, G. Tan, H. Gao, L. Li, R. Chen and F. Wu, *Small Methods*, 2022, **6**, 2200555.
- 141 R. Wang, S. Wu, F. Zhang, X. Zhao, Z. Lin, C.-Z. Wang and K.-M. Ho, *Phys. Chem. Chem. Phys.*, 2020, **22**, 13975–13980.
- 142 H. Liu, F. C. Strobridge, O. J. Borkiewicz, K. M. Wiaderek, K. W. Chapman, P. J. Chupas and C. P. Grey, *Science*, 2014, **344**, 1252817.
- 143 J. Wang and X. Sun, *Energy Environ. Sci.*, 2015, **8**, 1110–1138.
- 144 M. Morcrette, J. B. Leriche, S. Patoux, C. Wurm and C. Masquelier, *Electrochem. Solid-State Lett.*, 2003, **6**, A80.

- 145 Z. Jian, C. Yuan, W. Han, X. Lu, L. Gu, X. Xi, Y.-S. Hu, H. Li, W. Chen, D. Chen, Y. Ikuhara and L. Chen, *Adv. Funct. Mater.*, 2014, **24**, 4265–4272.
- 146 R. Thangavel, D. Han, B. Moorthy, B. K. Ganesan, M. Moorthy, Y. Park, K.-W. Nam and Y.-S. Lee, *Small Methods*, 2022, **6**, 2100888.
- 147 Y.-R. Wang, Y. Yang, Y.-L. Nie, Q. Wang, S. Liu and Q. Wang, *J. Energy Storage*, 2024, **83**, 110629.
- 148 G. Yao, X. Zhang, Y. Yan, J. Zhang, K. Song, J. Shi, L. Mi, J. Zheng, X. Feng and W. Chen, *J. Energy Chem.*, 2020, **50**, 387–394.
- 149 W. Yang, Q. Liu, L. Hou, Q. Yang, D. Mu, G. Tan, L. Li, R. Chen and F. Wu, *Small*, 2024, **20**, 2306595.
- 150 P. Barpanda, J. N. Chotard, N. Recham, C. Delacourt, M. Ati, L. Dupont, M. Armand and J. M. Tarascon, *Inorg. Chem.*, 2010, **49**, 7401–7413.
- 151 R. Tripathi, T. N. Ramesh, B. L. Ellis and L. F. Nazar, *Angew. Chem., Int. Ed.*, 2010, **122**, 8920–8924.
- 152 J. L. Pizarro-Sanz, J. M. Dance, G. Villeneuve and M. I. Arriortua-Marcaida, *Mater. Lett.*, 1994, **18**, 327–330.
- 153 C. Xu, J. Zhao, C. Yang and Y.-S. Hu, *ACS Cent. Sci.*, 2023, **9**, 1721–1736.
- 154 P. S. Camacho, R. Wernert, M. Duttine, A. Wattiaux, A. Rudola, P. Balaya, F. Fauth, R. Berthelot, L. Monconduit, D. Carlier and L. Croguennec, *ACS Appl. Mater. Interfaces*, 2021, **13**, 42682–42692.
- 155 W. Wang, Z. Hu, Z. Yan, J. Peng, M. Chen, W. Lai, Q.-F. Gu, S.-L. Chou, H.-K. Liu and S.-X. Dou, *Energy Storage Mater.*, 2020, **30**, 42–51.
- 156 A. Zhou, W. Cheng, W. Wang, Q. Zhao, J. Xie, W. Zhang, H. Gao, L. Xue and J. Li, *Adv. Energy Mater.*, 2020, 2000943.
- 157 L. Wang, J. Song, R. Qiao, L. A. Wray, M. A. Hossain, Y. D. Chuang, W. Yang, Y. Lu, D. Evans, J. J. Lee, S. Vail, X. Zhao, M. Nishijima, S. Kakimoto and J. B. Goodenough, *J. Am. Chem. Soc.*, 2015, **137**, 2548–2554.
- 158 W. Wang, Y. Gang, Z. Hu, Z. Yan, W. Li, Y. Li, Q.-F. Gu, Z. Wang, S.-L. Chou, H.-K. Liu and S.-X. Dou, *Nat. Commun.*, 2020, **11**, 980.
- 159 M. Blangero, D. Carlier, M. Pollet, J. Darriet, C. Delmas and J.-P. Doumerc, *Phys. Rev. B: Condens. Matter Mater. Phys.*, 2008, **77**, 184116.
- 160 A. K. Rai, L. T. Anh, J. Gim, V. Mathew and J. Kim, *Ceram. Int.*, 2014, **40**, 2411–2417.
- 161 S. C. Han, H. Lim, J. Jeong, D. Ahn, W. B. Park, K.-S. Sohn and M. Pyo, *J. Power Sources*, 2015, **277**, 9–16.
- 162 J. Braconnier, C. Delmas and P. Hagenmuller, *Mater. Res. Bull.*, 1982, **17**, 993–1000.
- 163 W. Ko, M.-K. Cho, J. Kang, H. Park, J. Ahn, Y. Lee, S. Lee, S. Lee, K. Heo, J. Hong, J.-K. Yoo and J. Kim, *Energy Storage Mater.*, 2022, **46**, 289–299.
- 164 X. Zhang, J. Chen, J. Ye, T. Zhang and Z. Hou, *Adv. Energy Mater.*, 2023, **13**, 2204413.
- 165 M. S. Chae, H. J. Kim, H. Bu, J. Lyoo, R. Attias, B. Dlugatch, M. Oliel, Y. Gofer, S.-T. Hong and D. Aurbach, *Adv. Energy Mater.*, 2020, **10**, 2000564.
- 166 L. Rakočević, S. Štrbac, J. Potočnik, M. Popović, D. Jugović and I. S. Simatović, *Ceram. Int.*, 2021, **47**, 4595–4603.
- 167 A. Caballero, L. Hernán, J. Morales, L. Sánchez, J. Santos Peña and M. A. G. Aranda, *J. Mater. Chem.*, 2002, **12**, 1142–1147.
- 168 X. Li, X. Ma, D. Su, L. Liu, R. Chisnell, S. P. Ong, H. Chen, A. Toumar, J. C. Idrobo, Y. Lei, J. Bai, F. Wang, J. W. Lynn, Y. S. Lee and G. Ceder, *Nat. Mater.*, 2014, **13**, 586–592.
- 169 A. Langella, A. Massaro, A. B. Muñoz-García and M. Pavone, *Chem. Mater.*, 2024, **36**, 2370–2379.
- 170 E. J. Kim, T. Hosaka, K. Kubota, R. Tatara, S. Kumakura and S. Komaba, *ACS Appl. Energy Mater.*, 2022, **5**, 12999–13010.
- 171 J. M. Paulsen and J. R. Dahn, *Solid State Ionics*, 1999, **126**, 3–24.
- 172 X. Liu, W. Zuo, B. Zheng, Y. Xiang, K. Zhou, Z. Xiao, P. Shan, J. Shi, Q. Li, G. Zhong, R. Fu and Y. Yang, *Angew. Chem., Int. Ed.*, 2019, **58**, 18086–18095.
- 173 X. Wang, Q. Zhang, C. Zhao, H. Li, B. Zhang, G. Zeng, Y. Tang, Z. Huang, I. Hwang, H. Zhang, S. Zhou, Y. Qiu, Y. Xiao, J. Cabana, C.-J. Sun, K. Amine, Y. Sun, Q. Wang, G.-L. Xu, L. Gu, Y. Qiao and S.-G. Sun, *Nat. Energy*, 2024, **9**, 184–196.
- 174 B. Peng, Y. Chen, L. Zhao, S. Zeng, G. Wan, F. Wang, X. Zhang, W. Wang and G. Zhang, *Energy Storage Mater.*, 2023, **56**, 631–641.
- 175 H. Yoshida, N. Yabuuchi, K. Kubota, I. Ikeuchi, A. Garsuch, M. Schulz-Dobrick and S. Komaba, *Chem. Commun.*, 2014, **50**, 3677–3680.
- 176 J. Xu, D. H. Lee, R. J. Clément, X. Yu, M. Leskes, A. J. Pell, G. Pintacuda, X.-Q. Yang, C. P. Grey and Y. S. Meng, *Chem. Mater.*, 2014, **26**, 1260–1269.
- 177 K. Sada, S. Kmiec and A. Manthiram, *Angew. Chem., Int. Ed.*, 2024, e202403865.
- 178 D. Kim, S.-H. Kang, M. Slater, S. Rood, J. T. Vaughey, N. Karan, M. Balasubramanian and C. S. Johnson, *Adv. Energy Mater.*, 2011, **1**, 333–336.
- 179 T. Liu, J. Liu, L. Li, L. Yu, J. Diao, T. Zhou, S. Li, A. Dai, W. Zhao, S. Xu, Y. Ren, L. Wang, T. Wu, R. Qi, Y. Xiao, J. Zheng, W. Cha, R. Harder, I. Robinson, J. Wen, J. Lu, F. Pan and K. Amine, *Nature*, 2022, **606**, 305–312.
- 180 W. He, W. Guo, H. Wu, L. Lin, Q. Liu, X. Han, Q. Xie, P. Liu, H. Zheng, L. Wang, X. Yu and D.-L. Peng, *Adv. Mater.*, 2021, **33**, 2005937.
- 181 Z. Jian, H. Yu and H. Zhou, *Electrochem. Commun.*, 2013, **34**, 215–218.
- 182 R. Kataoka, T. Mukai, A. Yoshizawa and T. Sakai, *J. Electrochem. Soc.*, 2013, **160**, A933–A939.
- 183 Y. Zhu, Y. Xu, Y. Liu, C. Luo and C. Wang, *Nanoscale*, 2013, **5**, 780–787.
- 184 H. Ma, B. Zhao, J. Bai, P. Wang, W. Li, Y. Mao, X. Zhu, Z. Sheng, X. Zhu and Y. Sun, *Adv. Sci.*, 2023, **10**, 2203552.
- 185 H. Huang, Y. Xia, Y. Hao, H. Li, C. Wang, T. Shi, X. Lu, M. W. Shahzad, B. B. Xu and Y. Jiang, *Adv. Funct. Mater.*, 2023, **33**, 2305109.
- 186 L. Wang, P. Zuo, G. Yin, Y. Ma, X. Cheng, C. Du and Y. Gao, *J. Mater. Chem. A*, 2015, **3**, 1569–1579.
- 187 P. Zuo, G. Cheng, L. Wang, Y. Ma, C. Du, X. Cheng, Z. Wang and G. Yin, *J. Power Sources*, 2013, **243**, 872–879.

- 188 W. Weppner, H. Schulz, C. Delmas, A. Nadiri and J. L. Soubeyroux, *Solid State Ionics*, 1988, **28**, 419–423.
- 189 C. Delmas, F. Cherkaoui, A. Nadiri and P. Hagenmuller, *Mater. Res. Bull.*, 1987, **22**, 631–639.
- 190 Y. Uebou, T. Kiyabu, S. Okada and J.-i. Yamaki, *The Reports of Institute of Advanced Materials Study*, 2002, vol. 16, p. 1.
- 191 K. Liang, H. Zhao, J. Li, X. Huang, S. Jia, W. Chen and Y. Ren, *Small*, 2023, **19**, 2207562.
- 192 D. H. Yun, J. Song, J. Kim, J. K. Seo, J. Kang, S. Park, J. Kim, D.-J. Yoo and S. Choi, *J. Mater. Chem. A*, 2023, **11**, 5540–5547.
- 193 Y. U. Park, D. H. Seo, H. S. Kwon, B. Kim, J. Kim, H. Kim, I. Kim, H. I. Yoo and K. Kang, *J. Am. Chem. Soc.*, 2013, **135**, 13870–13878.
- 194 P. Barpanda, M. Ati, B. C. Melot, G. Rousse, J. N. Chotard, M. L. Doublet, M. T. Sougrati, S. A. Corr, J. C. Jumas and J. M. Tarascon, *Nat. Mater.*, 2011, **10**, 772–779.
- 195 M. Reynaud, G. Rousse, A. M. Abakumov, M. T. Sougrati, G. Van Tendeloo, J.-N. Chotard and J.-M. Tarascon, *J. Mater. Chem. A*, 2014, **2**, 2671.
- 196 V. D. Neff, *J. Electrochem. Soc.*, 1978, **125**, 886–887.
- 197 Y. You, X.-L. Wu, Y.-X. Yin and Y.-G. Guo, *Energy Environ. Sci.*, 2014, **7**, 1643–1647.
- 198 T. Matsuda and Y. Moritomo, *Appl. Phys. Express*, 2011, **4**, 047101–047103.
- 199 F. M. Maddar, D. Walker, T. W. Chamberlain, J. Compton, A. S. Menon, M. Copley and I. Hasa, *J. Mater. Chem. A*, 2023, **11**, 15778–15791.
- 200 D. O. Ojwang, L. Häggström, T. Ericsson, R. Mogensen and W. R. Brant, *Dalton Trans.*, 2022, **51**, 14712–14720.
- 201 M. Xia, T. Liu, N. Peng, R. Zheng, X. Cheng, H. Zhu, H. Yu, M. Shui and J. Shu, *Small Methods*, 2019, **3**, 1900119.
- 202 M. Bianchini, F. Fauth, N. Brisset, F. Weill, E. Suard, C. Masquelier and L. Croguennec, *Chem. Mater.*, 2015, **27**, 3009–3020.
- 203 Z. Lu and J. R. Dahn, *J. Electrochem. Soc.*, 2001, **148**, A1225.
- 204 S.-M. Oh, S.-T. Myung, J.-Y. Hwang, B. Scrosati, K. Amine and Y.-K. Sun, *Chem. Mater.*, 2014, **26**, 6165–6171.
- 205 M. Sathiya, K. Hemalatha, K. Ramesha, J. M. Tarascon and A. S. Prakash, *Chem. Mater.*, 2012, **24**, 1846–1853.
- 206 K. Chihara, A. Kitajou, I. D. Gocheva, S. Okada and J.-i. Yamaki, *J. Power Sources*, 2013, **227**, 80–85.
- 207 Z. Liu, Y.-Y. Hu, M. T. Dunstan, H. Huo, X. Hao, H. Zou, G. Zhong, Y. Yang and C. P. Grey, *Chem. Mater.*, 2014, **26**, 2513–2521.
- 208 R. A. Shakoob, D.-H. Seo, H. Kim, Y.-U. Park, J. Kim, S.-W. Kim, H. Gwon, S. Lee and K. Kang, *J. Mater. Chem.*, 2012, **22**, 20535.
- 209 P. Ghigna and E. Quartarone, *J. Phys.: Energy*, 2021, **3**, 032006.
- 210 Y. Wang, L. Wang, H. Zhu, J. Chu, Y. Fang, L. Wu, L. Huang, Y. Ren, C.-J. Sun, Q. Liu, X. Ai, H. Yang and Y. Cao, *Adv. Funct. Mater.*, 2020, **30**, 1910327.
- 211 J. Y. Huang, L. Zhong, C. M. Wang, J. P. Sullivan, W. Xu, L. Q. Zhang, S. X. Mao, N. S. Hudak, X. H. Liu, A. Subramanian, H. Fan, L. Qi, A. Kushima and J. Li, *Science*, 2010, **330**, 1515–1520.
- 212 S.-H. Bo, X. Li, A. J. Toumar and G. Ceder, *Chem. Mater.*, 2016, **28**, 1419–1429.
- 213 L. Wang, A. Dai, W. Xu, S. Lee, W. Cha, R. Harder, T. Liu, Y. Ren, G. Yin, P. Zuo, J. Wang, J. Lu and J. Wang, *J. Am. Chem. Soc.*, 2020, **142**, 14966–14973.
- 214 L. Wang, T. Liu, A. Dai, V. De Andrade, Y. Ren, W. Xu, S. Lee, Q. Zhang, L. Gu, S. Wang, T. Wu, H. Jin and J. Lu, *Nat. Commun.*, 2021, **12**, 5370.
- 215 L. Wang, J. Wang, X. Zhang, Y. Ren, P. Zuo, G. Yin and J. Wang, *Nano Energy*, 2017, **34**, 215–223.
- 216 Y. Xie, H. Wang, G. Xu, J. Wang, H. Sheng, Z. Chen, Y. Ren, C.-J. Sun, J. Wen, J. Wang, D. J. Miller, J. Lu, K. Amine and Z.-F. Ma, *Adv. Energy Mater.*, 2016, **6**, 1601306.
- 217 X. Xu, M. Yan, X. Tian, C. Yang, M. Shi, Q. Wei, L. Xu and L. Mai, *Nano Lett.*, 2015, **15**, 3879–3884.
- 218 Y. Xie, H. Wang, G. Xu, J. Wang, H. Sheng, Z. Chen, Y. Ren, C.-J. Sun, J. Wen, J. Wang, D. J. Miller, J. Lu, K. Amine and Z.-F. Ma, *Adv. Energy Mater.*, 2016, **6**, 1601306.
- 219 Q.-C. Wang, Z. Shadike, X.-L. Li, J. Bao, Q.-Q. Qiu, E. Hu, S.-M. Bak, X. Xiao, L. Ma, X.-J. Wu, X.-Q. Yang and Y.-N. Zhou, *Adv. Energy Mater.*, 2021, **11**, 2003455.
- 220 Y. Xie, H. Gao, R. Harder, L. Li, J. Gim, H. Che, H. Wang, Y. Ren, X. Zhang, L. Li, Z. Chen, K. Amine and Z.-F. Ma, *ACS Appl. Energy Mater.*, 2020, **3**, 6107–6114.
- 221 O. Y. Gorobtsov, H. Hirsh, M. Zhang, D. Sheyfer, L. H. B. Nguyen, S. D. Matson, D. Weinstock, R. Bouck, Z. Wang, W. Cha, J. Maser, R. Harder, Y. S. Meng and A. Singer, *Adv. Energy Mater.*, 2023, **13**, 2203654.
- 222 P. Ji, X. Lei and D. Su, *Small Methods*, 2024, 2301539.
- 223 H. Li, S. Guo and H. Zhou, *J. Energy Chem.*, 2021, **59**, 191–211.
- 224 A. Van der Ven, Z. Deng, S. Banerjee and S. P. Ong, *Chem. Rev.*, 2020, **120**, 6977–7019.
- 225 Y. Mo, S. P. Ong and G. Ceder, *Chem. Mater.*, 2014, **26**, 5208–5214.
- 226 S. P. Ong, V. L. Chevrier, G. Hautier, A. Jain, C. Moore, S. Kim, X. H. Ma and G. Ceder, *Energy Environ. Sci.*, 2011, **4**, 3680–3688.
- 227 F. Ding, H. Wang, Q. Zhang, L. Zheng, H. Guo, P. Yu, N. Zhang, Q. Guo, F. Xie, R. Dang, X. Rong, Y. Lu, R. Xiao, L. Chen and Y.-S. Hu, *J. Am. Chem. Soc.*, 2023, **145**, 13592–13602.
- 228 A. Van der Ven and G. Ceder, *Electrochem. Solid-State Lett.*, 2000, **3**, 301–304.
- 229 F. Boucher, J. Gaubicher, M. Cuisinier, D. Guyomard and P. Moreau, *J. Am. Chem. Soc.*, 2014, **136**, 9144–9157.
- 230 V. Kapoor, B. Singh, G. Sai Gautam, A. K. Cheetham and P. Canepa, *Chem. Mater.*, 2022, **34**, 3373–3382.
- 231 P. A. Aparicio and N. H. de Leeuw, *Phys. Chem. Chem. Phys.*, 2020, **22**, 6653–6659.
- 232 E. Olsson and Q. Cai, in *Sodium-Ion Batteries*, 2022, pp. 259–300, DOI: [10.1002/9783527825769.ch9](https://doi.org/10.1002/9783527825769.ch9).
- 233 R. Tripathi, S. M. Wood, M. S. Islam and L. F. Nazar, *Energy Environ. Sci.*, 2013, **6**, 2257.